Bulletin of the Seismological Society of America, 92, 1, pp. 138–160, February 2002

Estimating Slip Distribution for the İzmit Mainshock from Coseismic GPS, ERS-1, RADARSAT, and SPOT Measurements

by Kurt L. Feigl, Francesco Sarti, Hélène Vadon, Simon McClusky, Semih Ergintav, Philippe Durand, Roland Bürgmann, Alexis Rigo, Didier Massonnet, and Rob Reilinger

Abstract We use four geodetic satellite systems (Global Positioning System [GPS], European Remote Sensing [ERS], RADARSAT, and Satellite Pour l'Observation de la Terre [SPOT]) to measure the permanent deformation field produced by the İzmit earthquake of 17 August 1999. We emphasize measurements from interferometric analysis of synthetic aperture radar (SAR) images acquired by ERS and RADARSAT and their geodetic uncertainties. The primary seismological use of these data is to determine earthquake source parameters, such as the distribution of slip and the fault geometry. After accounting for one month's postseismic deformation, tropospheric delay, and orbital gradients, we use these data to estimate the distribution of slip at the time of the İzmit mainshock. The different data sets resolve different aspects of the distribution of slip at depth. Although these estimates agree to first order with those derived from surface faulting, teleseismic recordings, and strong motion, careful comparison reveals differences of 40% in seismic moment. We assume smooth parameterization for the fault geometry and a standard elastic dislocation model. The root mean square residual scatter is 25 mm and 11 mm for the ERS and RADARSAT range changes, respectively. Our estimate of the moment from a joint inversion of the four geodetic data sets is $M_0 = 1.84 \times 10^{20}$ N m, a moment magnitude of M_w 7.50. These values are lower than other estimates using more realistic layered earth models. Given the differences between the various models, we conclude that the real errors in the estimated slip distributions are at the level of 1 m. The prudent geophysical conclusion is that coseismic slip during the İzmit earthquake tapers gradually from approximately 2 m under the Hersek delta to 1 m at a point 10 km west of it. We infer that the Yalova segment west of the Hersek delta may remain capable of significant slip in a future earthquake.

Introduction

The İzmit earthquake of 17 August 1999 was the first earthquake to generate a coseismic displacement field measured by four geodetic satellite systems: Global Positioning System (GPS), European Remote Sensing (ERS), RADARSAT, and Satellite Pour l'Observation de la Terre (SPOT). As such, it provides a unique opportunity for calibrating the interferometric analysis of synthetic aperture radar (SAR) measurements and estimating the earthquake source parameters. In view of the intense interest in this earthquake, we consciously seek to complement, rather than duplicate, previous work. Reilinger *et al.* (2000) used the GPS data to measure and model both coseismic and postseismic deformation for the İzmit event. We concentrate on the coseismic slip, leaving the detailed analysis of the postseismic deformation to other studies (Bürgmann *et al.,* 2002; Ergintav *et al.,* 2002; Hearn *et al.,* 2002). The same GPS network later captured the coseismic deformation for the 12 November Düzce earthquake (Ayhan *et al.,* 2001; Bürgmann *et al.,* 2002). Here, we consider only the İzmit event. Using four different ERS interferograms, Wright *et al.* (2001) estimated the fault geometry and the slip distribution, including slip triggered on two secondary faults. Inverting the ERS-2 interferogram, strong-motion accelerograms and teleseismic seismograms (separately and jointly), Delouis *et al.* (2002) estimated the slip distribution in both time and space. Buchon *et al.* (2001) solved the same problem using the strong-motion recordings only, and Yaki and Kikuchi (2000) used both the strong-motion and teleseismic recordings. Concentrating on the geodetic data only, we add the RADARSAT measurements and the SPOT correlation map calculated by Vadon and Massonnet (2000) to the ERS and GPS data sets. Taken together, these data measure six different components of the static coseismic displacement field (Fig. 1). In our inversions, we do not allow the slip distribution

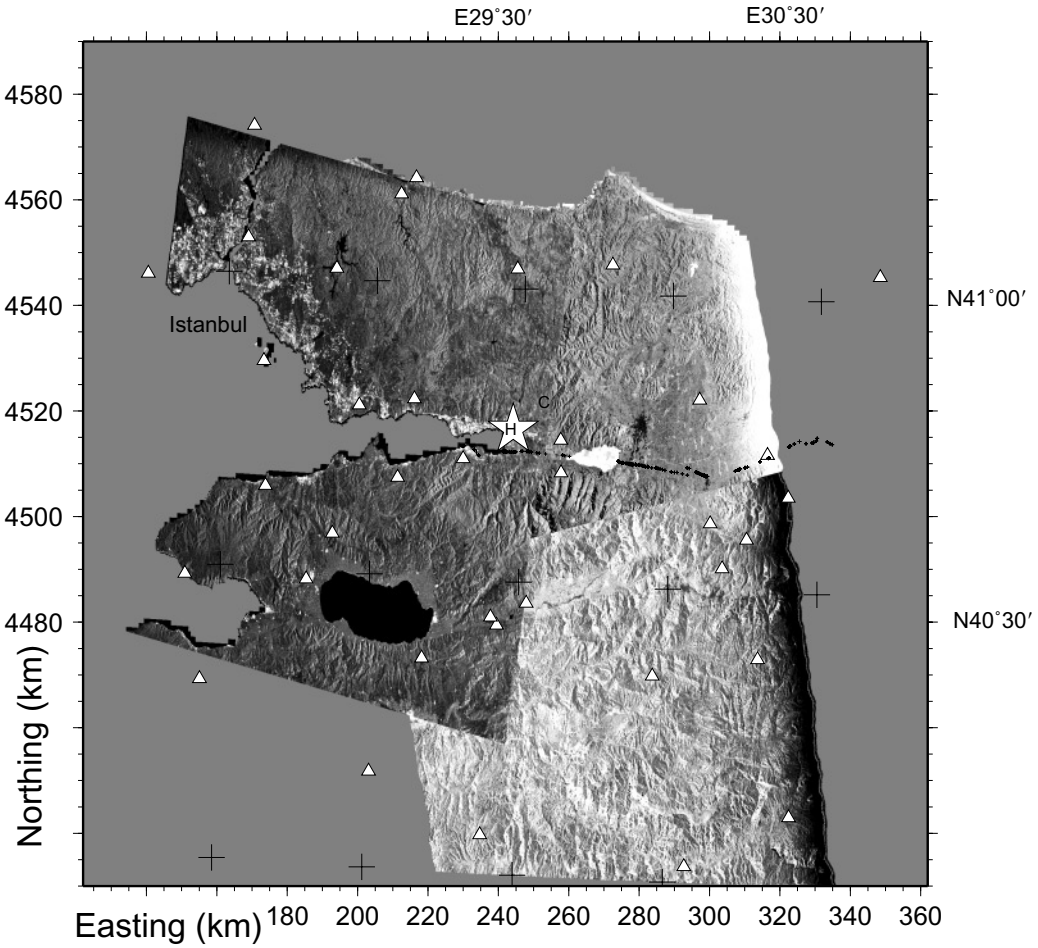

Figure 1. Location map showing conventional epicenter (star) at N40.76°, E29.97° as determined by the Kandilli Observatory from first motions (cited in Delouis *et al.* 2002) showing SAR backscatter (amplitude) images acquired by RADARSAT (left swath) and ERS-1 (right swath). Coordinates are easting and northing in km using the Universal Transverse Mercator projection, zone 36 (Snyder, 1982).

to vary in time. We do, however, admit the possibility of systematic errors, such as tropospheric artifacts and orbital gradients, in the interferograms.

The surface rupture caused by this earthquake has been mapped in the field (Barka, 1999; Barka *et al.,* 1999; Çemen *et al.,* 2000). We complement the preliminary surface rupture map with a trace digitized from the correlation of two optical SPOT satellite images (Vadon and Massonnet, 2000) and from the correlation of two ERS radar backscatter (amplitude) images (Sarti *et al.,* 2000). The conventional epicenter is indicated by a star in Figure 1.

One of the underlying motivations for all these studies is to evaluate the seismic hazard near Istanbul. Using Coulomb theory to calculate stress transfer, Hubert-Ferrari *et al.* (2000), Parsons *et al.* (2000), and Hearn *et al.* (2002) found that the İzmit earthquake increased the likelihood of earthquakes at both ends of the rupture trace. Yet these calculations rely heavily on reliable determinations of the source parameters, particularly the fault geometry and the slip gradient. This sensitivity motivates us to find robust estimate for these parameters.

Types of Geodetic Data

GPS Displacement Vectors. We use the GPS displacement vectors published previously by Reilinger *et al.* (2000). These authors estimated them using data from a GPS network of continuous stations and survey-mode benchmarks established prior to the earthquake (Straub *et al.,* 1997; Ayhan *et al.,* 1999; Yalcin *et al.,* 1999; McClusky *et al.,* 2000). Five continuous GPS stations were operating prior to the İzmit earthquake within the coseismic deformation field. Fifty-one GPS sites were resurveyed within two weeks of the İzmit mainshock to measure coseismic displacements (Ergintav *et al.,* 2002).

Reilinger *et al.* (2000) analyzed the GPS data following standard procedures using the GAMIT/GLOBK GPS processing software (Herring, 1991; King and Bock, 1997) as de-

scribed elsewhere (McClusky *et al.,* 2000). To estimate coseismic displacements, Reilinger *et al.* (2000) used a simple, linear-in-time model for elastic strain accumulation to extrapolate the prequake measurement of station position to the instant just before the İzmit event. Similarly, they used another elastic model for postseismic afterslip to extrapolate positions measured after the earthquake backward in time to the instant just after the mainshock. The result is a set of instantaneous coseismic displacement vectors for 17 August. In principle, they include no postseismic deformation. These corrected measurements of the east, north, and up components of displacements at 48 stations form the 144 data points in data set *G* (for GPS). The measurement errors include the uncertainties in the rates. The measurements and their uncertainties are available as an electronic supplement on the Internet at *www.sciencemag.org* (Reilinger *et al.,* 2000).

INSAR Range Changes from ERS-1. Although GPS records three components of the coseismic displacement vector **u** of a benchmark, INSAR records only the component along the line of sight between the satellite and ground point. The line of sight between the point on the ground and the radar satellite in the sky defines the unit vector $\hat{\mathbf{s}}$. For the ERS-1, its east, north, and upward components are -0.371, -0.087, $+0.925$, respectively, at the epicenter. The change in range $\Delta\rho$ or the distance measured along the line of sight between the satellite and ground point is $\Delta\rho = -u \cdot \hat{\mathbf{s}}$. Note that the sign convention is such that an upward movement will produce a positive value of $\mathbf{u} \cdot \hat{\mathbf{s}}$ and a negative value of $\Delta\rho$ (i.e., a decrease in range). Consequently, a purely horizontal east–west displacement of $|\mathbf{u}| = 75$ mm at the epicenter will produce a range change of $\Delta\rho$ of one 28-mm fringe in the interference pattern.

In our inversions, we consider only the 35-day coseismic ERS-1 interferogram, that is, the phase difference between images acquired on 12 August (orbit number 42229) and on 16 September (42730). It is the best available coseismic interferometric pair, as previously described by Reilinger *et al.* (2000). They published it as their figure 5A.

Our interferograms were calculated using the same raw SAR data from the European Space Agency (ESA), the same DIAPASON software (Centre National d'Etudes Spatiales [CNES], 1997), the same digital elevation model (DEM) calculated from ERS tandem pairs (Fielding *et al.,* 1999), and the same filtering algorithm (Goldstein and Werner, 1998) as used by Wright *et al.* (2001). The ERS-1 interferogram of Wright *et al.* (2001) differs from ours only in width, orbital parameters, and the fringe points sampled by manual unwrapping. In contrast, Delouis *et al.* (2002) used the ERS-2 interferogram, the ROI_PAC software, and automatic wrapping to build an INSAR data set for inversion in combination with strong-motion recordings and teleseismic seismograms. Armijo *et al.* (1999) and Çakir *et al.* (2001) also considered the same 12 August–16 September interferogram, adding surface rupture data and geomorphological observations. Despite their similarities, the numerous versions of the few usable coseismic interferograms for the İzmit mainshock differ in important ways that we can use to infer the nature of the uncertainty budget for INSAR measurements.

Before using these interferograms to estimate the source parameters of the İzmit earthquake, we must understand them, both qualitatively and quantitatively. Thoroughly addressing these issues in an uncertainty budget is the primary geodetic objective in this article. First, we interpret the interferogram qualitatively to understand how different effects contribute to the fringe pattern. Many instructive examples appear in review articles by Massonnet and Feigl (1998), Madsen and Zebker (1998), and Bürgmann *et al.* (2000). The mathematical details appear in another review (Bamler and Hartl, 1998). For the İzmit earthquake, the most important effects involve the time interval, topographic relief, orbital trajectories, and tropospheric refraction, apparently in combination.

The ERS-1 interferogram spans a time interval ending 29 days after the mainshock. We assume that this interferogram contains up to 20 mm of postseismic range change, based on the postquake GPS measurements and postseismic modeling (Reilinger *et al.,* 2000). There are at least two possible approaches to resolve the discrepancy in time interval between the GPS and INSAR measurements. The simplest approach is to neglect the difference, assuming that ERS interferograms record essentially coseismic deformation, as do Delouis *et al.* (2002), Armijo *et al.* (1999), and Çakir *et al.* (2001). Our approach uses a one-fault postseismic slip model to predict the first 29 days of postseismic deformation (Reilinger *et al.,* 2000). These corrections are then subtracted from the ERS-1 measurements to obtain a purely coseismic set of range changes pertaining to the instant of the mainshock rather than an interval of time.

The correlation in both interferograms is fairly good outside the agricultural areas in the valley floor because the temporal separation is only 35 days. Thus changes in the ground cover are small.

In addition, the separation between orbital trajectories was minimized in an orbital maneuver following the İzmit mainshock. Rather than adjust the velocity of the satellite to follow its nominal trajectory, ESA's European Space Operations Center used their regularly scheduled maneuver in September to match the August trajectories. Such a rapid response in an operational satellite system is laudable and requires excellent lines of communication between the seismological community and the space agencies.

As a result of the small orbital separation, the ERS interferograms are fairly insensitive to topography. To quantify the topographic effect, we use the altitude of ambiguity h_a defined by Massonnet and Rabaute (1993) as the shift in altitude needed to produce one topographic fringe. For the ERS-1 interferogram, its value is $h_a = 336$ m at the epicenter. Even if Fielding's DEM contains errors of the order of $\varepsilon \sim 50$ m, they would produce a phase error of only $\varepsilon/h_a \sim 1/8$ fringe or 4 mm in range in the ERS-1 interferogram. As

a result, we can safely neglect the effect of topographic errors in the ERS-1 interferogram.

Shortcomings in modeling the orbital trajectories can still leave small artifacts in the interferograms. Our experience with the preliminary ORRM trajectories leads us to expect several orbital fringes (~100 mm in range) across a 100-km scene, for a proportional error of $\sim 10^{-6}$ in the range-change measurements. This error usually appears as a gradient or planar fringe ramp in the interferogram. In most cases, these artifactual orbital fringes run roughly parallel to the satellite's ground track, striking more north–south than east–west. To prevent the orbital errors from biasing our slip estimates, we admit a gradient in the interferogram. This involves adding two nuisance parameters to the estimation procedure: an eastward derivative $\partial(\Delta\rho)/\partial x$ and northward derivative $\partial(\Delta\rho)/\partial y$. These apply only to the INSAR data. We estimate two such gradient parameters for the ERS-1 data set and two more for the RADARSAT data set.

Tropospheric artifacts also contaminate the ERS-1 and ERS-2 interferograms, as we have argued previously (Reilinger *et al.,* 2000). Since the interferometric fringes hug the topography like contour lines, they may be caused by the interplay between tropospheric layering and topographic relief. These artifacts can exceed 50 mm in range, as apparent in a comparison of the ERS and GPS estimates of coseismic range change (Fig. 2). Artifacts of this size are also corroborated by estimating tropospheric delay parameters from the two GPS receivers operating at the time of the ERS-1 passes (note 46 in *Reilinger et al.* [2000]), by comparing independent ERS-1 and ERS-2 interferograms (figure 7 in *Reilinger et al.* [2000]), and by a one-day interferogram acquired before the mainshock (Fig. 3).

Separating the tropospheric noise from the deformation signal can be very difficult, particularly when both are correlated with topographic relief (e.g., Rigo and Massonnet, 1999). Indeed, variations in the refractive index of the troposphere remain the dominant source of error in the INSAR technique (Goldstein, 1995; Massonnet and Feigl, 1995; Rosen *et al.,* 1996; Tarayre and Massonnet, 1996; Zebker *et al.,* 1997; Hanssen, 1998; Hanssen, 2001). The hugging effect was first observed as several concentric fringes in a one-day interferogram on Mount Etna (Massonnet *et al.,* 1995; Delacourt *et al.,* 1998; Beauducel *et al.,* 2000). One can recognize this subtle effect using pairwise logic (Massonnet and Feigl, 1995) or using a DEM and local meteorological observations (Delacourt *et al.,* 1998; Williams *et al.,* 1998).

To mitigate the effect of the tropospheric artifacts on our estimates of the coseismic slip distribution, we implicitly assume a uniform troposphere. We then estimate the (negative) correlation between tropospheric delay along the radar line of sight and the topographic elevation. As a free nuisance parameter in our estimation procedure, this so-called topo-tropo scale factor applies only to the INSAR range changes. This parameterization differs slightly from the layered tropospheric model employed by Beauducel *et al.* (2000). Our approach adds only one free parameter to the inversion, whereas their approach adds one parameter per tropospheric layer. Yet neither approach allows horizontal variations in tropospheric delay. Such variations could contribute, however, to the horizontal gradients we estimate to account for orbital errors. The essential point is to reduce the trade-off between the nuisance parameters and those of interest in the fault model.

To use the radar interferograms as data in an inverse problem requires an unambiguous measurement of the range change, which implies unwrapping the interferogram. For the İzmit interferogram, we simply count and digitize the fringe pattern. Although tedious, this technique avoids errors because the human eye is very good at following colored fringes, even where they are noisy. It also recognizes areas where the fringes become too noisy to count. On the other hand, Delouis *et al.* (2002) were able to unwrap their interferogram using an automatic procedure to sample the deformation field on a regular grid.

Even unwrapped, radar range changes are still only relative measurements. To make them absolute, we must identify the fringe corresponding to zero deformation. In our joint inversions, we do this by estimating additive constants. Like Delouis *et al.* (2002), we must estimate two such parameters: one on the north side and another on the south side of the fault trace because we cannot follow an interferometric fringe across the fault. The radar correlation breaks down in the Gulf of Marmara and the cultivated valley floor including the fault trace. Consequently, the difference between these two nuisance parameters trades off almost perfectly with the total slip on the fault unless we include GPS vectors in the inversion.

INSAR Range Changes from RADARSAT. We also consider a RADARSAT interferogram that reaches from the epicenter to Istanbul. Shown in Figure 4, it is the phase difference between images acquired on 16 August (orbit number 19731) and on 3 October (20417). The altitude of ambiguity h_a for this pair is 46 m. Both images were acquired in descending passes using standard mode in swath 7 with an incidence angle between 44° and 49° from vertical. The unit vector $\hat{\mathbf{s}}$ along the line of sight between the point on the ground and the RADARSAT satellite in the sky has east, north, and upward components of 0.694, 0.114, and 0.711, respectively, at the epicenter. This vector forms an angle of 66° with the ERS unit vector. Consequently, a range change $\Delta\rho$ of one 28-mm fringe in the RADARSAT interference pattern corresponds to $|\mathbf{u}| = 40$ mm of purely horizontal east–west displacement at the epicenter.

To calculate this interferogram, we followed essentially the same procedures as for the ERS-1 data. Orbital information can be extracted from the header file or requested from the Canadian Space Agency or RadarSat International prior to ordering. The state vectors are given every 8 min in an inertial reference system, starting at the equator. One file contains 15 such samples, spanning slightly more than one orbital cycle. Using a Hermitian spline, we interpolated the

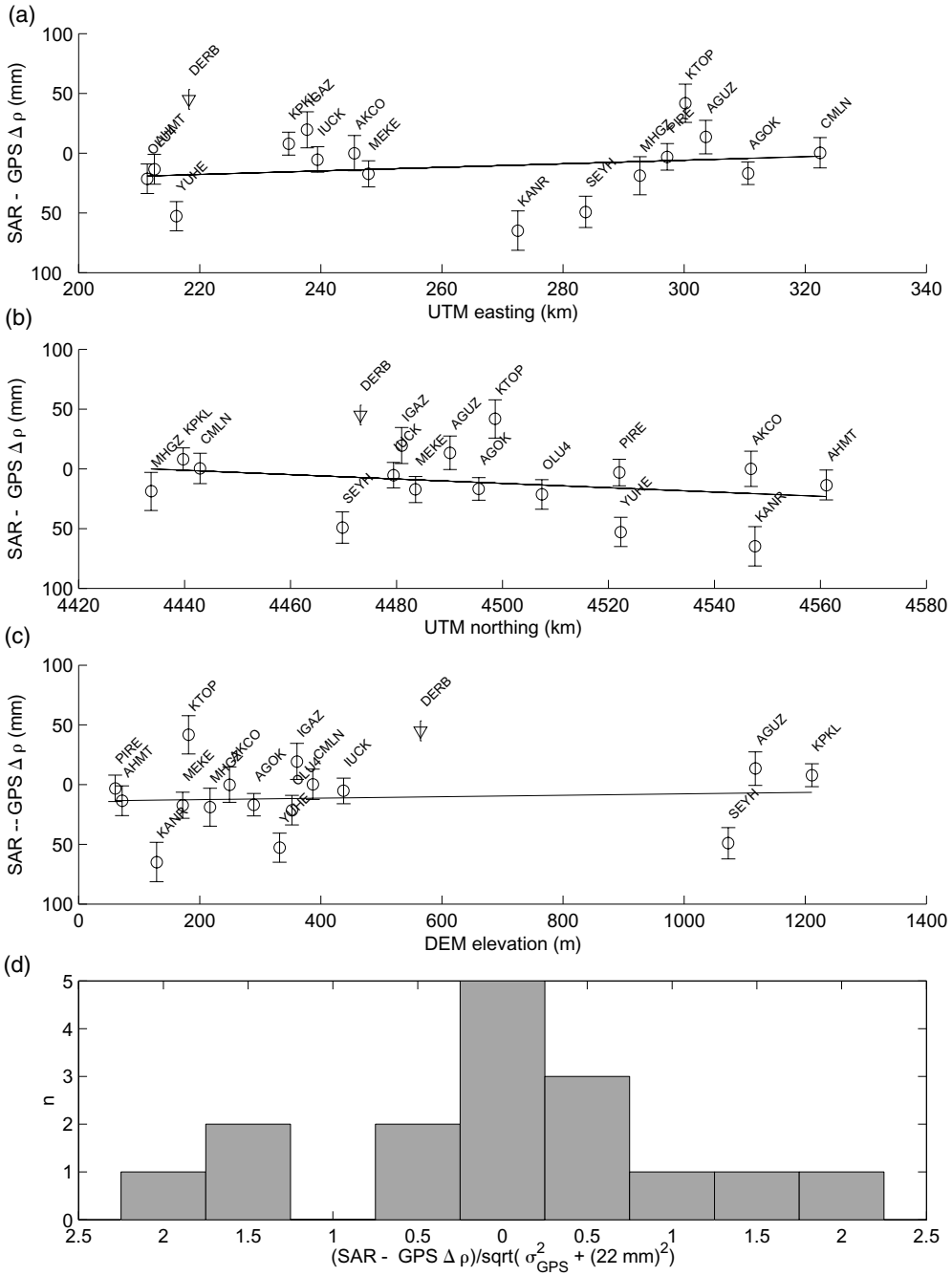

Figure 2. Differences in range change between those measured in the ERS-1 interferogram and those calculated from the GPS displacement vectors (Reilinger *et al.,* 2000) shown in profiles as a function of (a) easting, (b) northing, and (c) elevation. We consider the DERB estimate to be an outlier and exclude it from the statistics. We suspect the vertical components of the GPS measurements at KTOP, KANR, YUHE, KDER, SEYH, SMAS, SISL, SILE, and KUTE. We multiply their uncertainties by a factor of 10 in the G data set. The slopes of the best-fitting lines are 0.14, −0.18, and 6.0 mm/km for the east, north, and upward profiles, respectively. (d) Histogram of the same ERS-GPS differences normalized by $(\sigma_G{}^2 + \sigma_E{}^2)^{1/2}$, assuming a standard deviation of $\sigma_E = 22$ mm for the ERS range-change measurements.

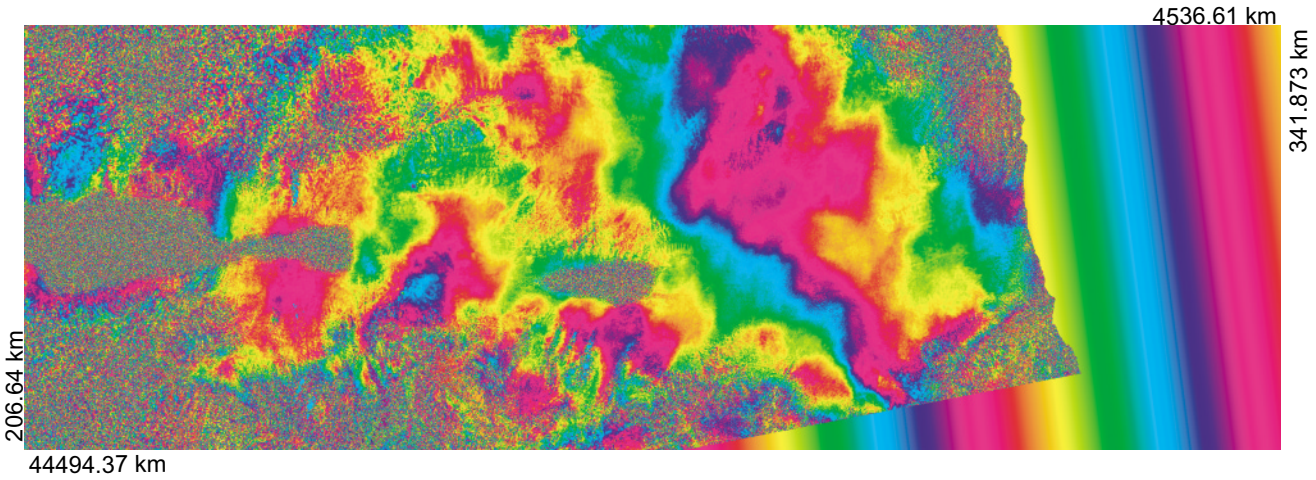

Figure 3. Interferogram showing the phase difference between an ERS1 image acquired 12 August 1999 (orbit number 42229) and an ERS-2 image acquired 13 August 1999 (orbit number 22556). The altitude of ambiguity h_a is 40 m, but the DEM used for this calculation has an estimated rms accuracy of about 7 m. Orbital fringes have been modeled empirically with a linear gradient. As a result, the remaining fringes must be tropospheric in origin.

orbits to 1-min sampling intervals in a terrestrial reference frame for input to the DIAPASON software.

Since none of the RADARSAT fringes cross the fault, their ability to resolve fault slip is limited. For the *R* data set, we use 159 digitized values on the northern side of the fault only, where the coseismic RADARSAT fringes extend well beyond the edge of our ERS-1 interferogram. Consequently, a single free parameter suffices to determine the constant value to be added to the range changes. In addition, we estimate three gradient parameters for the *R* data set, as for the *E* data set.

Correlation of Two Optical Images Acquired by the SPOT Satellite. It is also possible to detect (large) coseismic displacements by correlating two optical images. The lag vectors estimated between corresponding cells of a prequake and a postquake image measure the horizontal components of the coseismic displacement vector field with submeter precision and subhectometer resolution (Crippen, 1992; Crippen and Blom, 1992; Vadon and Massonnet, 2000; Van Puymbroeck *et al.,* 2000). To capture the İzmit earthquake of 17 August, we correlate optical images acquired by the SPOT4 satellite on 9 July and the SPOT2 satellite on 16 September (Vadon and Massonnet, 2000). After antialiasing resampling, the result is a measurement of the offset between the two images at each 20-m pixel where the correlation succeeds. In this case, lines of the SPOT images are almost parallel to the fault, so we use only the offset in image columns to determine the horizontal component of displacement in the direction S77°E. In other words, this data set measures the projection of the displacement field along the horizontal unit vector with east, north, and upward components ($+0.974$, -0.225, 0, respectively).

The two images were acquired in very similar geometric configurations with a small angle between their viewing vectors. Nonetheless, the correlation map still shows the effects of slight differences in spacecraft position and sensor attitude. These we model empirically with a biquadratic polynomial fit. After median filtering with a 100- by 100-m window, we map the measurements into cartographic coordinates using an affine transformation (Fig. 5). This map shows a discontinuity corresponding to the trace of the surface rupture mapped between the east end of the bay at İzmit and Sapanca Lake. The mean offset between two 5- by 20-km blocks on opposite sides of the fault is 4.60 ± 0.24 m. After median filtering with a 2- by 2-km window, we retain 148 values as traced in Figure 6 in the *S* (for SPOT) data set. We correct them for 35 days of postseismic deformation, as for the ERS data.

Correlation of Two SAR Backscatter Images Acquired by the ERS Satellites. A similar correlation technique also applies to SAR images. By correlating two single look complex (SLC) SAR amplitude (backscatter) images acquired at different times, Michel *et al.* (1999) measured ground displacements for the Landers earthquake. Their result is a "two-dimensional displacement field with independent measurements about every 128 m in azimuth and 250 m in range. The accuracy depends on the characteristics of the images. For the Landers test case discussed in the study, the 1-σ uncertainty is 0.8 m in range and 0.4 m in azimuth" (Michel *et al.,* 1999, p. 875). Furthermore, these authors claim that "this measurement provides a map of major surface fault ruptures accurate to better than 1 km and an information on coseismic deformation comparable to the 92 GPS measurements available. Although less accurate, this technique is

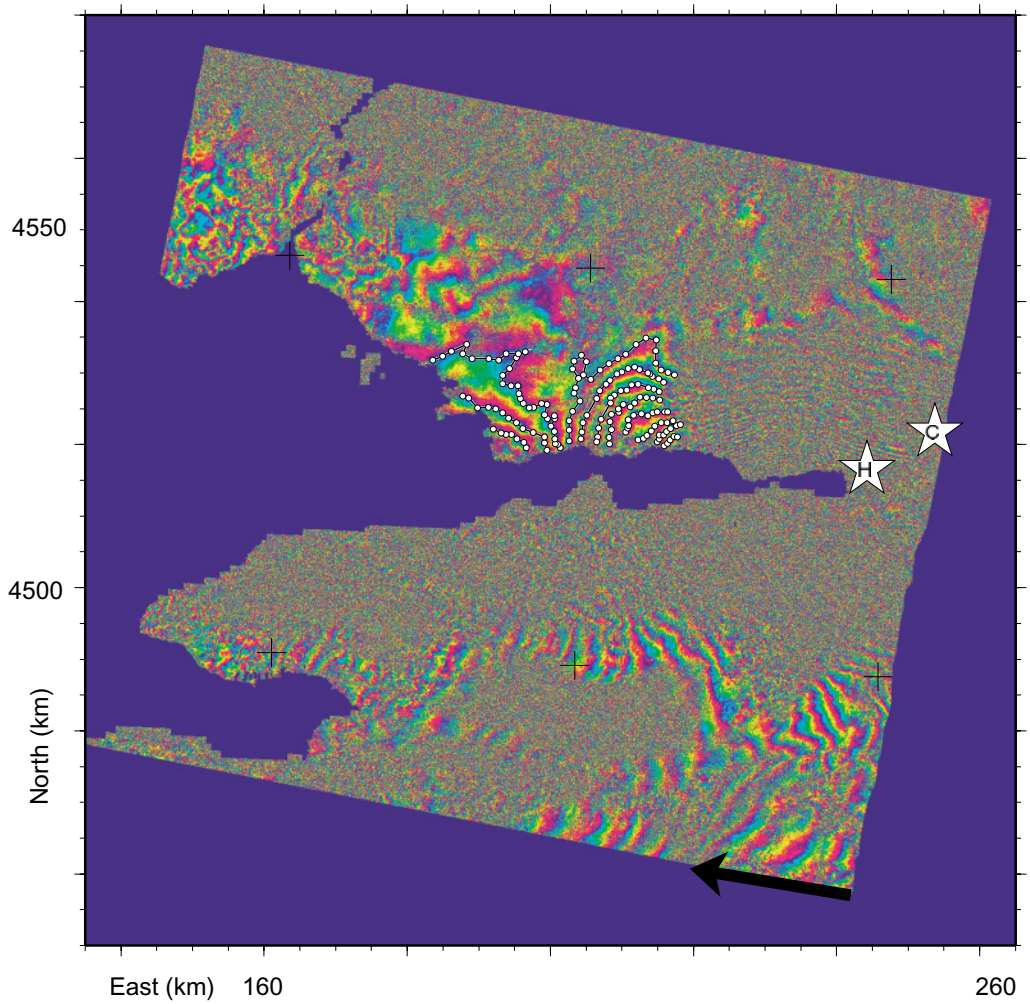

Figure 4. Interferogram showing the phase difference between RADARSAT images acquired 16 August (orbit number 19731) and on 3 October (20417). The altitude of ambiguity h_a for this pair is 46 m. White circles show locations of the 159 digitized values retained in the *R* data set. Stars denote hypocenter (H) and centroid (C) locations. The arrow denotes the horizontal projection of the radar "look" vector from satellite to ground.

more robust than SAR interferometry and provides complementary information since interferograms are only sensitive to the displacement in range" (Michel *et al.,* 1999, p. 875).

For İzmit, however, Sarti *et al.* (2000) found less accurate results. Having used multiple scales for their correlation cells, they found the range component of the coseismic displacement with a scatter in excess of 1 m. Indeed, it is difficult to discern even the trace of the fault in the map of ERS range offsets (Fig. 7). Consequently, we do not include these data in our inversion.

The Standard Elastic Half-Space Model

To explain the observed coseismic deformation, a simple model of a dislocation in an elastic half-space provides a good approximation. Okada (1985) derived the expressions for the coseismic (permanent) displacement **u** at the Earth's surface caused by a fault at depth in closed analytic form. Here we follow Okada's (1985) notation, as in Feigl and Dupré (1999). To describe a single fault element (also called a subfault or patch) as a dislocation requires 10 parameters. The fault patch has length L and width W. The slip on the fault plane is a vector **U** with three components, U_1, U_2, and U_3. The position coordinates of the fault patch are E, N, and d, taken positive east, north, and down, respectively. The azimuth α gives the strike of the fault in degrees clockwise from north. Finally, an observer facing along strike should see the fault dip at δ degrees to his right.

In each of our solutions, the only free model parameters are the along-strike components U_2 of the slip vector at each fault element. The other nine parameters are held fixed to their prior values for each element. These fixed parameters incorporate several important assumptions: a double-couple mechanism ($U_3 = 0$), pure, horizontal strike slip ($U_1 = 0$), a vertical fault ($\delta = 90°$) rupturing from the surface to $d =$

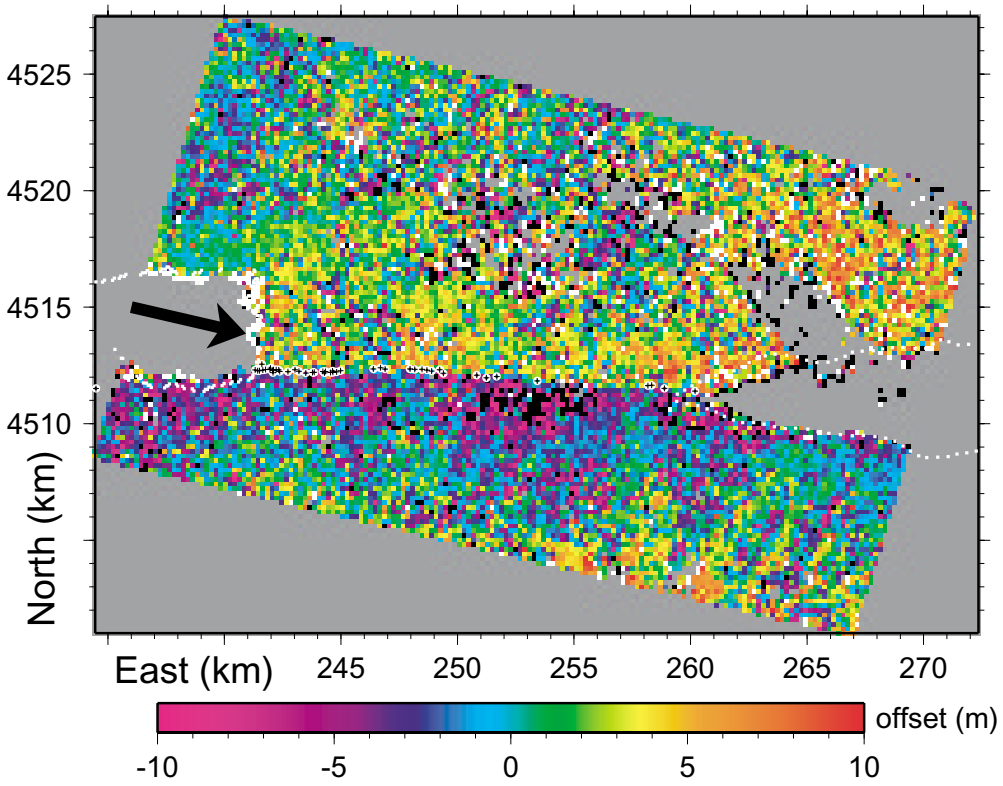

Figure 5. Component at S77°E of the coseismic displacement field measured by correlation of SPOT images acquired on 9 July and 16 September 1999 (Vadon and Massonnet, 2000). The black crosses on white disks represent the mapped trace of the surface rupture. The original 20-m pixels have been filtered using a two-dimensional median filter on a 100- by 100-m window.

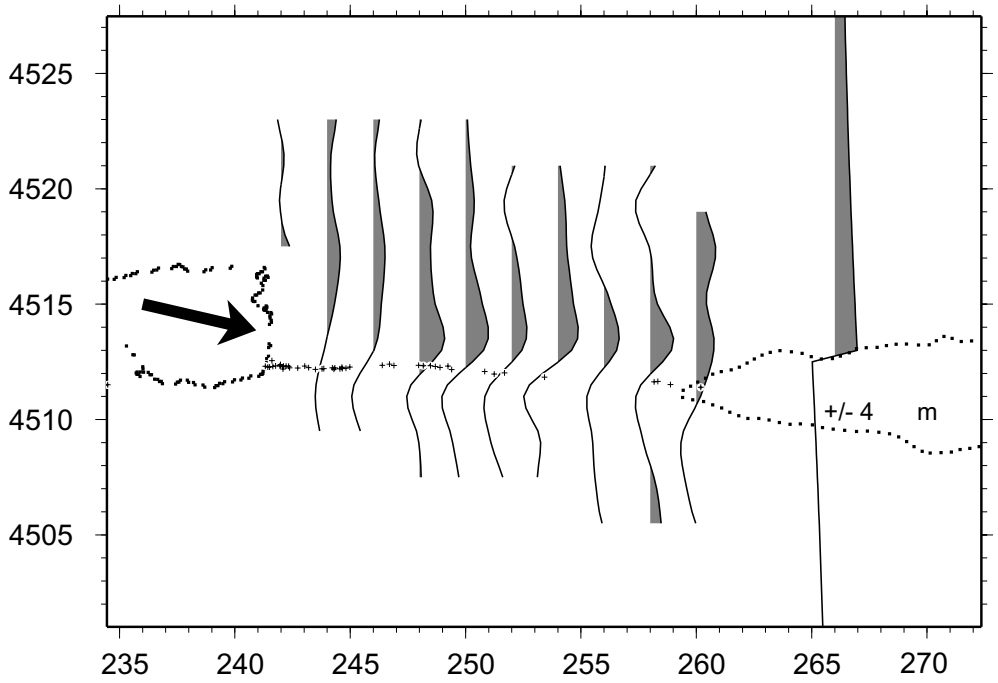

Figure 6. Component at S77°E of the coseismic displacement field measured by correlation of SPOT images. Positive values, representing displacement in the direction S77°E, are shaded. These values were extracted from the previous figure after application of a two-dimensional median filter on a 2- by 2-km window. The curves follow the points retained in the *S* data set for the inversion. The scale curve at right is calculated assuming 8 m of slip from the surface to 15 km depth. Other symbols as in previous figure.

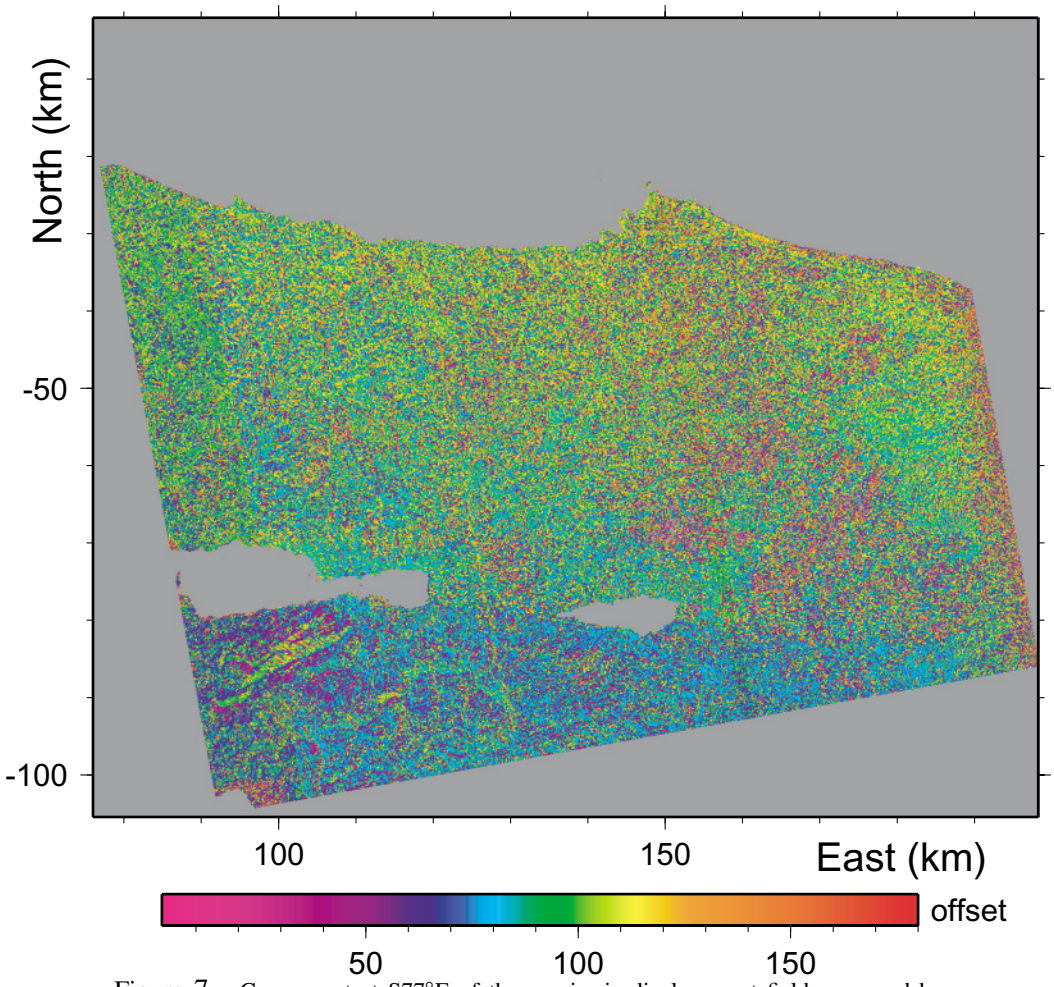

Figure 7. Component at S77°E of the coseismic displacement field measured by correlation of two ERS images, as described by Sarti *et al.* (2000). Note that the discontinuity in these measurements does not follow the mapped trace of the fault as well as the SPOT correlation map.

21-km depth, and a trace approximating the mapped surface rupture (Fig. 8).

The standard Okada model assumes that the Earth's surface is flat, corresponding to the bounding plane of the elastic half-space. The Lamé coefficients λ and μ specify the elastic medium. For simplicity, we assume that $\lambda = \mu$, so that these parameters drop out of the expressions for surface displacement. Such a medium, called a Poisson solid, has a Poisson's ratio of 1/4. We assume the shear modulus μ = 30 GPa (Feigl, 2002). Our assumptions differ slightly from those in other studies. Delouis *et al.* (2002) assume μ = 33 GPa, while Wright *et al.* (2000) assume μ = 34.3 GPa and λ = 32.2 GPa, implying a Poisson's ratio of 0.242.

Estimation Procedure

We seek to estimate two types of quantities: slip values on individual fault patches and nuisance parameters, such as gradients and offsets, needed to account for unmodeled systematic errors in the data sets. To estimate these parameters using least squares, we use a singular value decomposition (SVD) algorithm (Menke, 1989; Anderson *et al.,* 1992). To avoid spurious values typical of an oscillatory solution, we apply a smoothing operator. It minimizes the second spatial derivative (discrete Laplacian) of the slip distribution (Segall and Harris, 1987). We choose the weighting for this smoothing constraint by evaluating the trade-off between roughness and misfit and then use the same value for all data sets. We select a weighting that is rough enough to resolve some detail but smooth enough to inhibit backward (left-lateral) slip. This way, we need not apply additional smoothing by truncating the singular values.

One advantage of the SVD procedure is that it provides an estimate of the uncertainty of the estimates in the form of an *a posteriori* standard deviation of each model parameter. This we quote without multiplying by the normalized rms for the solution.

One disadvantage of the SVD approach is that it allows backward slip, namely, left-lateral slip in our case. A symp-

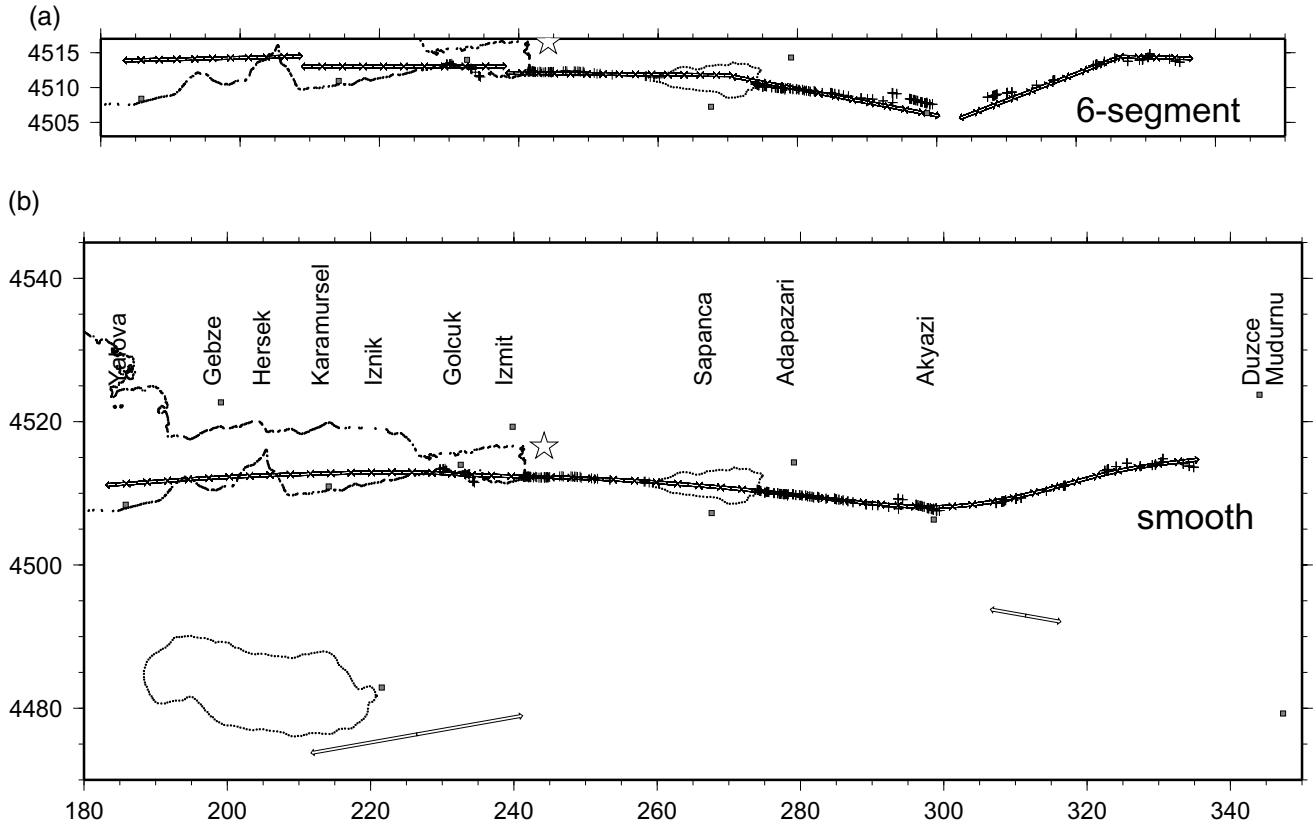

Figure 8. (a) Map of six-segment geometric parameterization as traced by Reilinger *et al.* (2000). Shown as arrows, this parameterization includes 56 lengths of 3 km along strike and 7 widths of 3 km in depth. (b) Smooth geometric parameterization, including 54 lengths of 3 km along strike and 7 widths of 3 km in depth for a total of 378 patches along the main strand of the North Anatolian Fault. In addition, we use one segment in the Mudurnu Valley and one segment to represent the Iznik fault, as proposed by Wright *et al.* (2000). Other features include mapped surface rupture (crosses) (Barka, 1999; Barka *et al.,* 1999; Çemen *et al.,* 2000), epicenter (star), coastline, and towns.

tom of poor resolution, this artifact tends to occur at the ends of the fault and at depth. To avoid it, we impose 0 ± 1 mm of slip at the ends of the faults and on the patches in the 18- to 21-km depth range. In the final joint *ERGS* solution, only 18 patches have more than 0.2 m of left-lateral slip.

Determining the Uncertainties in the Data

In solving this inverse problem, we expect to find a more reliable solution and a better estimate of the uncertainties if we correctly weight the different data sets (e.g., Barrientos and Ward, 1990; Holdahl and Sauber, 1994). In our case, we assume a diagonal covariance matrix. We will determine the appropriate standard deviations and thus the relative weighting for the *E, R*, and *S* data sets by comparison with the *G* data set.

Data Covariance Matrix for GPS Displacement Vectors

As a basis for comparison, we assume that the GPS uncertainties determined by Reilinger *et al.* (2000) are correct as published for the stations observed during survey campaigns. The standard deviation of the coseismic displacement vector at a typical benchmark ranges from 3 to 5 mm for the horizontal components and from 10 to 20 mm for the vertical components. At the continuous GPS stations (TUBI, DUMT, KANT, MERT, and MADT), we assign standard deviations of approximately 3 mm for the horizontal components and 10 mm for the vertical components. We neglect the correlations between the components and any correlations between stations.

To verify these uncertainties, we evaluate the residuals obtained by fitting a dislocation model to data set *G* alone. Their scatter is greater than expected. The rms scatter in the residuals is 32, 23, and 55 mm for the east, north, and vertical components, respectively (Table 1). We attribute most of the misfit to deficiencies in the model, as we discuss subsequently.

To avoid conflicts between the vertical components of the GPS-determined vectors and the mostly vertical ERS range changes, we have multiplied the standard deviations by a factor of 10 for the vertical components at nine GPS

Table 1
Models

Code	Remarks	Chi-Square per N	rms Residual (mm)						Moment*		File name
					GPS						
			ERS	RSAT	East	North	Up	SPOT	Estimate N.m	Sigma N.m	
6	GPS only, six-segment	5.5			35	33	54		1.65×10^{20}	2.63×10^{17}	g6a_burgmann5s
G	GPS only	5.9			32	23	55		1.84×10^{20}	1.65×10^{18}	g6a_sift21w8a.202
Gc	GPS only, no near field	4.3			21	15	60		1.73×10^{20}	1.64×10^{18}	g6l_sift21w8a.202
E	ERS only	5.7	28						1.57×10^{20}	7.23×10^{17}	g6b_sift21w8a.101
En	ERS only, nuisance‡	4.9	23						1.43×10^{20}	7.23×10^{17}	g6a_sift21w8a.101
R	RADARSAT	8.2		14					1.68×10^{20}	1.64×10^{18}	r3e_sift21w8a.101
Rn	RADARSAT, nuisance§	4.3		7					6.76×10^{19}	1.64×10^{19}	r3d_sift21w8a.201
S	SPOT only	36.7						1404	2.21×10^{19}	2.55×10^{18}	s5c_sift21w8a.101
Sn	SPOT only, nuisance‖	36.3						615	7.33×10^{19}	1.65×10^{19}	s5b_sift21w8a.201
GE		4.8	21		12	17	53		1.95×10^{20}	7.28×10^{17}	g6l_e6a_sift21w8a.201
GS		19.2			11	13	54	636	1.97×10^{20}	6.63×10^{18}	g6l_s5a_sift21w8a.201
GR		5		12	11	13	55		1.97×10^{20}	6.52×10^{18}	g6l_r3c_sift21w8a.201
REGS†		15.6	25	11	33	25	52	804	1.84×10^{20}	2.10×10^{18}	g6a_s5b_e6a_r3d_sift21w8a.205
REGcS†		15.8	24	12	13	20	55	811	1.68×10^{20}	2.12×10^{18}	g6j_s5b_e6a_r3d_sift21w8a.205

*Moment and unscaled uncertainty assume shear modulus $\mu = 30$ GPa.
†Nuisance parameters free: four offsets + six gradients.
‡Nuisance parameters free: two offsets + three gradients.
§Nuisance parameters free: one offset + three gradients.
‖Nuisance parameters free: one offset.

survey benchmarks: KTOP, KANR, YUHE, KDER, SEYH, SMAS, SISL, SILE, and KUTE. Most of them are within 10 km of the fault trace. Many of them disagree with the ERS estimates in range.

Measurement Uncertainty for ERS Range Changes

We compare the INSAR range changes with the projection of the GPS vectors along the ERS radar line of sight (Fig. 2). Compared to the GPS estimates, the rms difference is 30 and 42 mm along the radar line of sight for the ERS-1 and ERS-2 interferograms, respectively. To find the standard deviations σ_G for the GPS range determinations, we propagate the individual GPS uncertainties through the projection onto the radar line of sight. These uncertainties appear as vertical error bars in Figure 2. Of course, we can make this comparison only at those points that meet three conditions: (1) prequake GPS observation, (2) postquake GPS observation, and (3) fall in a coherent part of the coseismic interferograms. Only 17 points meet these conditions for our coseismic ERS-1 interferogram at İzmit. By focussing the raw images all the way to the last illuminated pixel, Wright *et al.* (2001) were able to extend their interferogram by 15 km to locate seven additional points, confirming a scatter of several centimeters in range. At Landers, the same type of comparison at nine points found an rms discrepancy of 34 mm in range between ERS-1 and the dual-frequency coseismic GPS measurements (Massonnet *et al.,* 1993; Massonnet and Feigl, 1998). Although such comparisons are painstaking, they can reveal blunders in the recordings of the GPS antenna heights. By using independent GPS measurements for calibration, these comparisons presumably yield the accuracy of the ERS range-change measurements, including any systematic effects but excluding the additive constant.

On the other hand, some of the discrepancy must be due to errors in the GPS measurements. Indeed, the ERS–GPS difference exceeds 100 mm in range at five points not shown in Figure 2 (SISL, KDER, GLCK, KUTE, and SMAS). At DERB, the ERS–GPS difference exceeds 3 standard deviations in range. After omitting these points and removing a linear trend, we find an rms difference of 27 mm between the ERS and GPS estimates of range change. By assigning a standard deviation of $\sigma_E = 22$ mm to the ERS range-change measurements, we can explain the scatter. The histogram of the ERS–GPS differences normalized by $(\sigma_G^2 + \sigma_E^2)^{1/2}$ looks like a normal distribution (Fig. 2). In this case, the chi-square statistic normalized by the degrees of freedom f is unity. Accordingly, we assign a standard deviation of 22 mm to all the ERS range-change measurements in the *E* data set.

To confirm our value for the measurement uncertainty, we invert the ERS measurements in the *E* data set alone. The residual range changes have an rms scatter of 23 mm. This solution, including five free nuisance parameters (two additive constants and three gradients), is called solution E_n in Table 1. It effectively uses the dislocation model as an empirical best fit to describe the data.

However, we know very little about how these measurements are correlated with one another. As a first approximation, we assumed the ERS measurements to be independent and set the *E* data covariance matrix to be diagonal, that is $(22 \text{ mm})^2$ times the identity matrix.

Measurement Uncertainty for SPOT Offset Maps

A priori, we assume a value of 63 cm for the standard deviation for a SPOT measurement, after averaging on a 2-km square pixel. We have determined this value from the residuals obtained by fitting a dislocation model to the union of data sets *G* and *S* (Table 1). In this *GS* solution, however, we also estimate one nuisance parameter—the additive constant. The rms scatter of the SPOT residuals in the *GS* solution is 636 mm. Similarly, in the S_n inversion of the *S* data set alone, we find an rms residual scatter of 615 mm.

This level of uncertainty is higher than we expected based on a null calibration. Applying the same technique to two images of the same ground scene taken at the same time by nearly identical instruments, we found typical rms scatters of 20–30 cm in the estimates of offset. In the İzmit case, both temporal decorrelation over the two months between acquisition epochs and the slight difference in the spectral bands of the two instruments are likely to increase the measurement uncertainty. Our uncertainty is also higher than the "accuracy of ~20 cm" that Van Puymbroeck *et al.* (2000, p. 3486) found at Landers by comparison to an elastic dislocation model.

As for the ERS data, we know very little about how the SPOT offset measurements are correlated with one another. As a first approximation, we assume that the filtered values are independent because they sample the displacement field on profiles 2 km apart. Thus, we take the covariance matrix for the *S* data set to be the identity matrix times (630 mm)^2. As a consequence, the SPOT observations carry very little weight (compared to the *G, E*, or *R* measurements) in the joint inversions.

Inversion Results

GPS Alone

Table 1 summarizes the solutions in terms of residual statistics and moments. Figure 9 shows the slip distribution estimated from the GPS data by Reilinger *et al.* (2000), assuming the six-segment fault geometry shown in Figure 8a. The characteristics of this slip distribution are (1) a peak of over 5 m of slip near Golcuk some 25 ± 5 km west of the hypocenter; (2) a peak of over 5 m of slip in the West Sapanca segment 10 km east of the hypocenter; (3) a peak of over 4 m of slip east of Sapanca some 38 km east of the hypocenter; (4) less than 4 m of slip some 43 ± 5 km west of the hypocenter (under the Hersek delta), decaying to less than 0 m some 50 km west of the hypocenter; (5) a pronounced gap with no resolvable slip between the East Sapanca and Karadere segments 50 and 60 km to the east of the hypocenter; (6) maximum slip at shallow (9 ± 3 km) depths; (7) shallow slip less than 3 m on the Karadere segment between 70 km east of the hypocenter, gradually decaying to less than 1 m some 80 km east of the hypocenter; (8) a gap with less than 2 m of slip between the West Sapanca and East Sapanca segments 20 to 30 km east of the hypocenter; and (8) a gap with less than 2 m of slip from 3

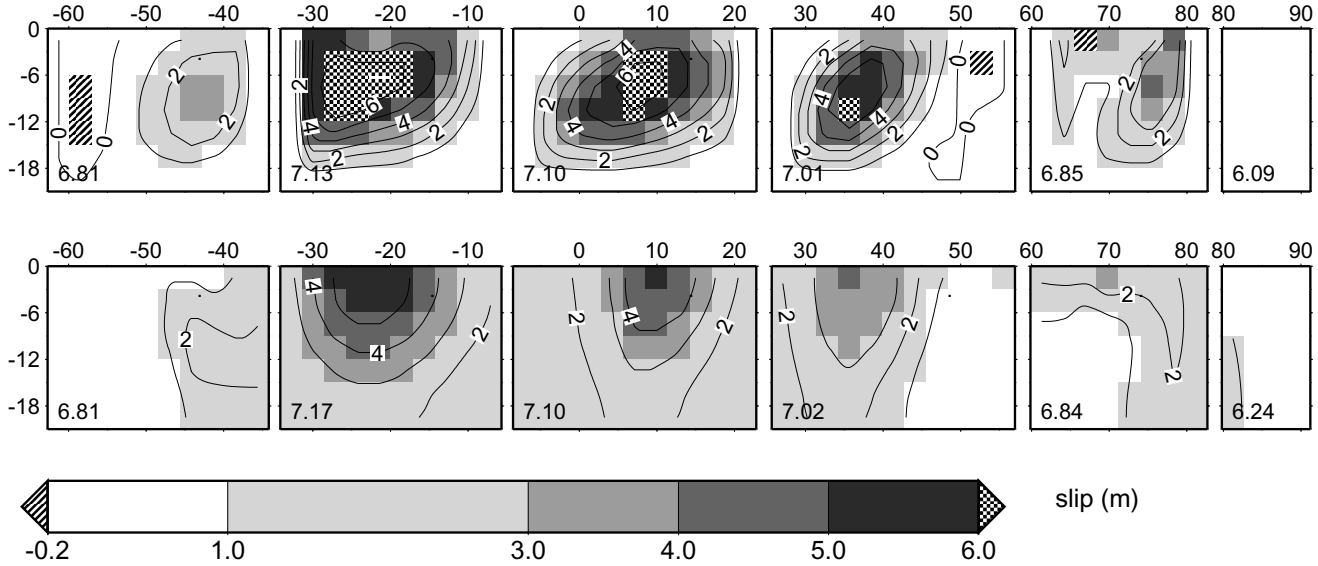

Figure 9. Slip distribution estimated from the GPS data alone by Reilinger *et al.* (2000), using the same six-segment geometry to parameterize the fault. The *x* axis is labeled with the horizontal coordinate in km along the fault trace relative to the conventional epicenter. The *y* axis is labeled with the vertical coordinate in km relative to the surface. From left (west) to right (east), these segments are named Yalova, Golcuk, West Sapanca, East Sapanca, West Karadere, and East Karadere.

to 10 km west of the hypocenter, between the West Sapanca and Golcuk segments.

The Effect of Geometry

One drawback of the six-segment fault model is the large displacements it predicts near the fault tips. Imposing a no-slip boundary condition mitigates this problem at the expense of realism at step-overs, such as the right-stepping extensional jogs at Golcuk (near km −7) and Hersek (near km −34).

Another drawback of a piecewise linear geometric parameterization is that the modeled fault segments can fall too close to geodetic measurements in the near field. This will lead to an overestimate of slip on the fault patch closest to the measurement point. Although this issue arises for the GPS benchmarks only at GLCK, KDER, SISL, OLU4, and SMAS, it becomes crucial for the imaging pixels. For example, the ERS fringes come within 5 km of the fault trace at its western termination near the Hersek delta. Similarly, both the SPOT and the ERS measurements are within 2 km in the hypocentral segment between İzmit and Lake Sapanca.

To minimize these problems, we choose another, smoother geometric parameterization for the fault trace that passes as close as possible to the mapped surface rupture (Fig. 8b). It also includes the Mudurnu Valley fault segment and the Iznik fault segment, where Wright *et al.* (2001) infer small amounts of triggered slip.

Using this smooth geometry with the GPS data alone, we find a slip distribution that retains the essential characteristics of Figure 9 from Reilinger *et al.* (2000). For example, Figure 10a shows that the slip at the western end of the fault drops to less than 2 m at a point 40 km west of the hypocenter (below the tip of the Hersek delta) and to less than 1 m some 13 km to the west, around km −53.

Compared to Reilinger *et al.* (2000), the main difference is that our bottom boundary condition prohibits slip below 18 km. Our smoothing constraint appears to be stronger than theirs because it causes a steeper gradient and more slip at the maxima. The notable differences in the slip distribution are that (1) the maximum slip values increase to 7 m, 6 m, and 5 m at the three peaks, (2) the slip peaks are deeper at 6- to 12-km depth than at the 0–6 km such that the centroid moves downward to 11-km depth, (3) the moment increases to $M_0 = 1.84 \times 10^{20}$ N m, and (4) the slip gap narrows between 50 and 60 km east of the epicenter, as the fit improves in the near-field GPS data at SISL and SMAS. The backward left-lateral slip in this gap appears to be a desperate attempt to fit the GPS vector at KDER, only 1 km from the fault trace. Here in the near field, our elastic dislocation model is a drastic simplification.

ERS Range-Change Data Only

Using the *E* data set, we perform two solutions. The first, with the five nuisance parameters free, is presented in the previous section as the E_n solution. Now, in the *E* solution, we hold them fixed to zero. Instead, we have corrected the *E* data set using the values of the nuisance parameters estimated in a joint solution called *GE,* which combines the *G* and *E* data sets. In the *E* solution, the residuals have an rms scatter of 21 mm, slightly better than the value of 23 mm we obtained for the E_n solution.

Figure 10b shows the slip distribution estimated from the ERS data alone in the *E* solution. It barely resolves the slip maxima in the Golcuk (km −23) and West Sapanca (km 9) segments. The maximum in the East Sapanca segment is smeared inside the 1-m contour reaching from km 40 to km 80. At the western end of the fault, the *E* inversion retrieves a vague 10-km-wide smear of less than 2 m of slip to the west of the tip of the Hersek Peninsula at km −43. The 2-m contour falls within 3 km of its position in the *G* solution.

The resolution is poor because the INSAR fringes do not cross the fault, which causes a trade-off between the nuisance parameters and the total fault slip. The $M_0 = 1.43 \times 10^{20}$ N m moment of the E_n solution, in which the nuisance parameters are free, is 9% smaller than the value we find in the *E* solution, in which they are fixed. At the other (eastern) end of the fault, the *E* data set resolves no more than 2 m of slip beyond 30 km from the epicenter, where the GPS data over 3 m around km 80. This seems to be a consequence of the lack of measurements in our *E* data set in this area. The moment for the *E* slip distribution is $M_0 = 1.57 \times 10^{20}$ N m, 15% smaller than for the *G* data set alone.

RADARSAT Range-Change Data Only

Using the *R* data set, we perform two solutions. The first has four free nuisance parameters: one offset and three gradients. This solution, called R_n, yields an rms residual scatter of 7 mm. The moment of $M_0 = 0.67 \times 10^{20}$ N m is 63% smaller than for the *G* solution. Second, in the *R* solution, we fix the nuisance parameters to zero, after correcting the RADARSAT data using the values of the nuisance parameters estimated in the *GR* solution. The *R* residuals have an rms scatter of 14 mm and a moment $M_0 = 1.68 \times 10^{20}$ N m, within 10% of the value we found in the *G* solution. The nuisance parameters are again trading off with the fault slip.

ERS-1, RADARSAT, and SPOT Data Sets Each Combined with the GPS Data Set

To test our assumptions about the relative weighting of the data sets, we invert each of the *E, R*, and *S* data sets in combination with the *G* data set. These solutions are called *GE, GR*, and *GS*, respectively. They yield misfits of 21 mm, 12 mm, and 636 mm in rms scatter for the *E, R*, and *S* residuals, respectively. These values, coupled with the almost unchanged rms scatter in the *G* residuals, confirm our choice of *a priori* standard deviations.

The *GE, GR*, and *GS* solutions also determine the nuisance parameters we apply to the data in used in the indi-

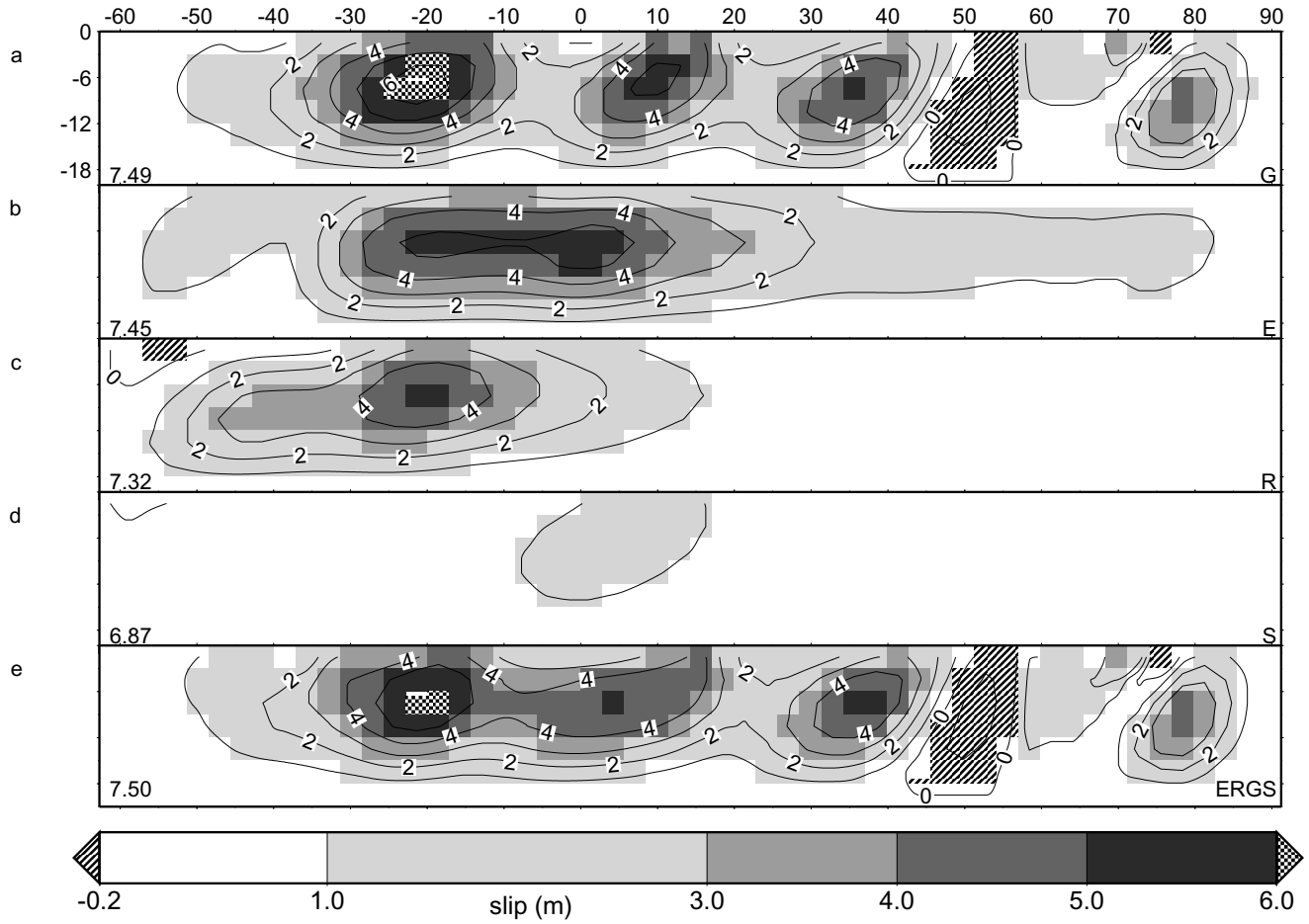

Figure 10. (a) Distribution of horizontal, right-lateral strike slip estimated from the GPS displacement vectors in the *G* data set alone using the using the smooth parameterization of the fault geometry. Horizontal axis gives distance along the fault trace in km from the epicenter estimated by Kandilli Observatory at N40.76°, E29.97° (Delouis *et al.,* 2002). On this scale, the point of the Hersek delta projects onto km 43. Vertical axis is depth in km. Contour interval is 1 m. (b) Slip distribution estimated from *E* data set extracted from the ERS-1 interferogram. The two offset and three gradient parameters are held fixed to the values estimated from the *GE* solution. (c) Slip distribution estimated from the *R* data set extracted from the RADARSAT interferogram. The offset and three gradient parameters are held fixed to the values estimated from the *GR* solution. (d) Slip distribution estimated from the offset measurements in the *S* data set extracted from the SPOT correlation map. The offset value is held fixed to the values estimated from the *GS* solution. (e) Slip distribution estimated from the *ERGS* data set including the GPS, ERS, RADARSAT, and SPOT observations.

vidual *E, R*, and *S* solutions we describe in the previous section and show in Figure 10b–d.

Combined ERS-1, RADARSAT, GPS, and SPOT Data Set

Figure 10e shows the slip distribution estimated from the combination of the *E, R, G*, and *S* data sets. This is our preferred solution and the one we interpret.

The residual rms misfits are 25 mm for the *E* subset, 11 mm for the *R* subset, and 804 mm for the *S* subset. These values are less than 3 mm above those determined for each data set individually. Similarly, the GPS residuals in the *ERGS* solution are less than 2 mm worse in rms than in the *G* solution. These results suggest that the relative weighting of the four data types is about right (Table 1). The small residual rms value for the *R* subset suggests that the nuisance parameters are absorbing misfit. Indeed, the small spatial extent of the digitized values we extracted from the coherent fringes on the north side of the fault seem to prevent meaningful estimates of the gradients or the offset for the *R* data set.

To evaluate this solution, we show the normalized residuals in Figure 11, map them in Figure 12, and profile them in Figure 13. We also use the *ERGS* solution to predict su-

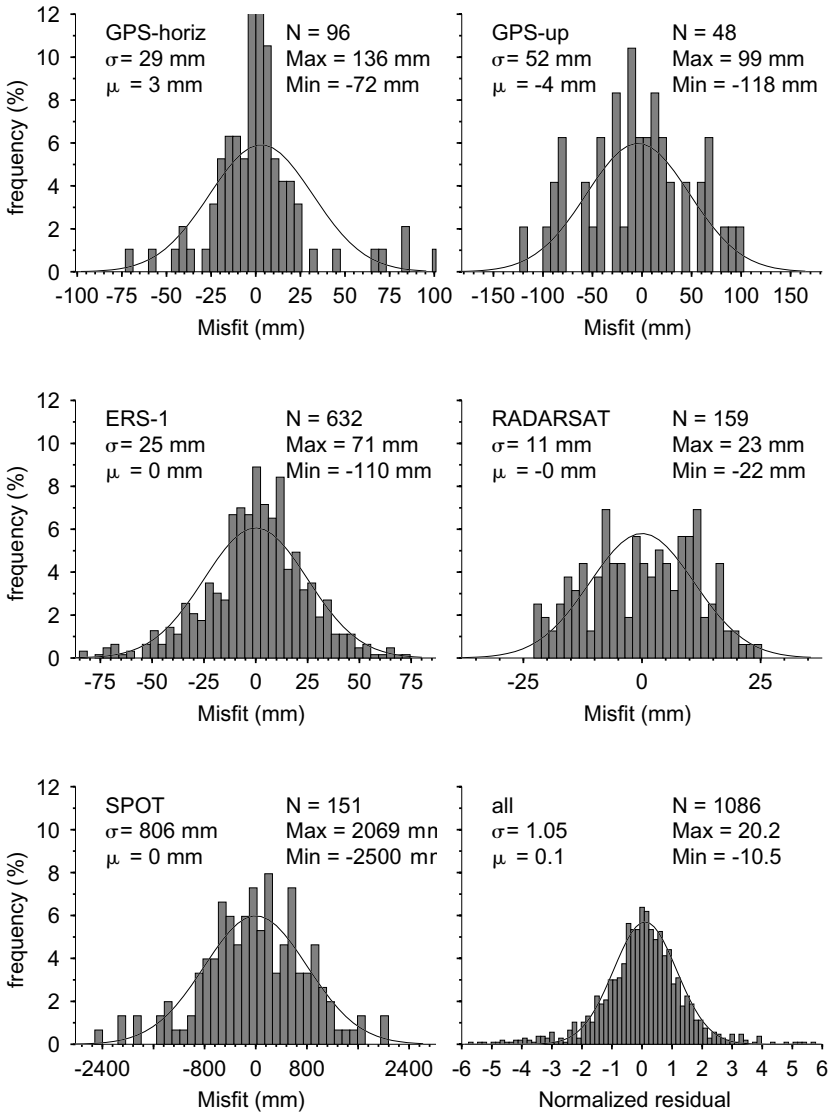

Figure 11. Histogram of residuals for the combined ERS, RADARSAT, GPS, and SPOT data subsets in the *ERGS* solution. The lower right panel shows the normalized residuals for the complete *ERGS* data set. For this panel, the curve and statistics exclude the outliers beyond 2 standard deviations from the mean.

persets of the data sets included in the inversions. Accordingly, Figure 14 shows the residual ERS-1 fringes calculated from the ERGS slip distribution and its associated nuisance parameters. Although it still shows fringe gradients, the majority of the signal has been explained. The remaining residual fringes appear to result from shortcomings in the model rather than random measurement noise, as we discuss subsequently.

The slip distribution estimated from the combined *ERGS* data set resembles the GPS-only solution. Compared to the *G* solution, the *ERGS* solution diminishes the size of the western slip maximum in the Golcuk segment. The peak in the combined *ERGS* solution at km -20 emphasizes the agreement between the *G, E*, and *R* solutions. Further west, around km -35, the combined *ERGS* solution compromises between the *E* solution, which barely resolves 1–2 m of slip, and the *R* and *G* solutions, which push for more than 3 m. East of the the hypocenter, between İzmit and Sapanca Lake, the slip maximum in the combined *ERGS* solution is broader than in the *G* solution. Again, this reflects a compromise between the *E, R*, and *S* solutions. The centroid is at N40.71°, E30.10°, over 10 km eastward along strike from the conventional epicenter.

Discussion

Gradients in the Interferograms

We find large artifactual gradients in the ERS interferograms. Indeed, the eastward and northward derivatives of

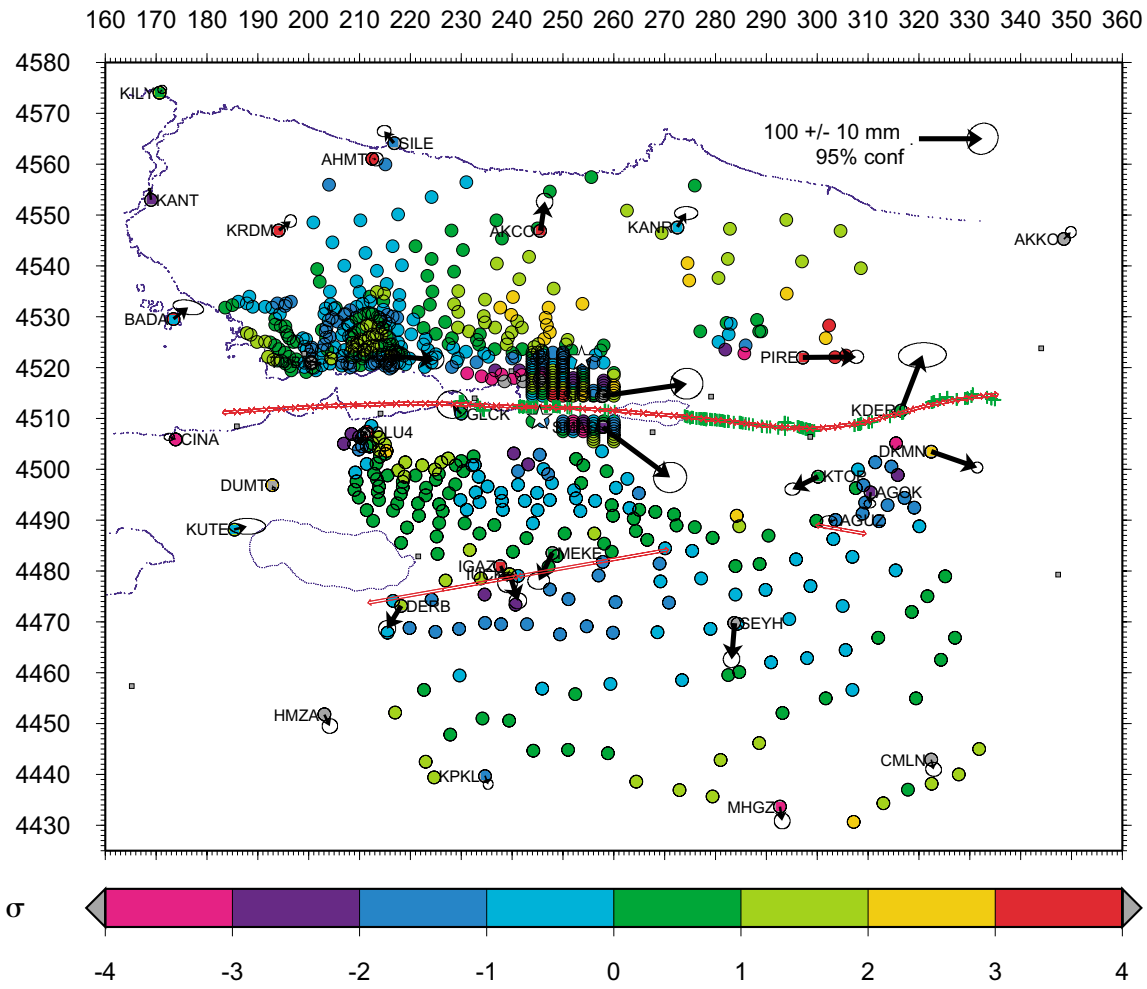

Figure 12. Map of normalized residuals for the EGS inversion. Colored circles denote ERS and SPOT normalized residuals, whereas squares denote the vertical component of the GPS normalized residuals, using the same color scale. Extreme outliers beyond 4 standard deviations from the mean are shown in gray. The residuals for the horizontal components of the GPS displacements are shown as black arrows with their 95% confidence error ellipses. Mapped surface rupture (green crosses) and modeled fault segments (red arrows).

range change are significant. In our preferred joint inversion (*ERGS*), we find values of $\partial(\Delta\rho)/\partial x = -0.5 \pm 0.03 \times 10^{-6}$ and $\partial(\Delta\rho)/\partial y = 1.7 \pm 0.04 \times 10^{-6}$ for these quantities in the *E* data set, respectively. These values are of the same order of magnitude as the slopes of the best-fitting lines in the profiles of ERS–GPS discrepancies (Fig. 2). Such large gradients are consistent with our experience with the preliminary ORRM orbits. The gradients imply almost two north-striking fringes spread over the 100-km east–west dimension of the interferogram, and over nine east-striking fringes spread over the 150-km north–south dimension of the interferogram. Left uncorrected, the former error could bias the along-strike variation of the slip distribution. Similarly, the latter effect would lead to an overestimate of the total amount of slip across the fault, and thus the moment. In our case, however, including the two horizontal gradients as nuisance parameters changes the moment by less than 1%.

We find horizontal gradients of the same order of magnitude for the RADARSAT data. In our preferred joint inversion (ERGS), we find values of $\partial(\Delta\rho)/\partial x = +5.2 \pm 0.1 \times 10^{-6}$ and $\partial(\Delta\rho)/\partial y = -8.6 \pm 0.3 \times 10^{-6}$ for the eastward and northward gradients in the *R* data set, respectively. That the uncertainties for these parameters are larger than for the *E* data set is a consequence of the small spatial extent of the *R* data set.

Tropospheric Effects

The most pronounced example of a tropospheric artifact appears as a residual of approximately 8 cm in range almost 50 km north of the fault when Delouis *et al.* (2002) included the ERS-2 interferogram in their inversion, as shown in profile P1 of their figure 12. As a systematic error, this type of artifact can perturb the slip estimates significantly. The inversion procedure is particularly sensitive to gradients in the

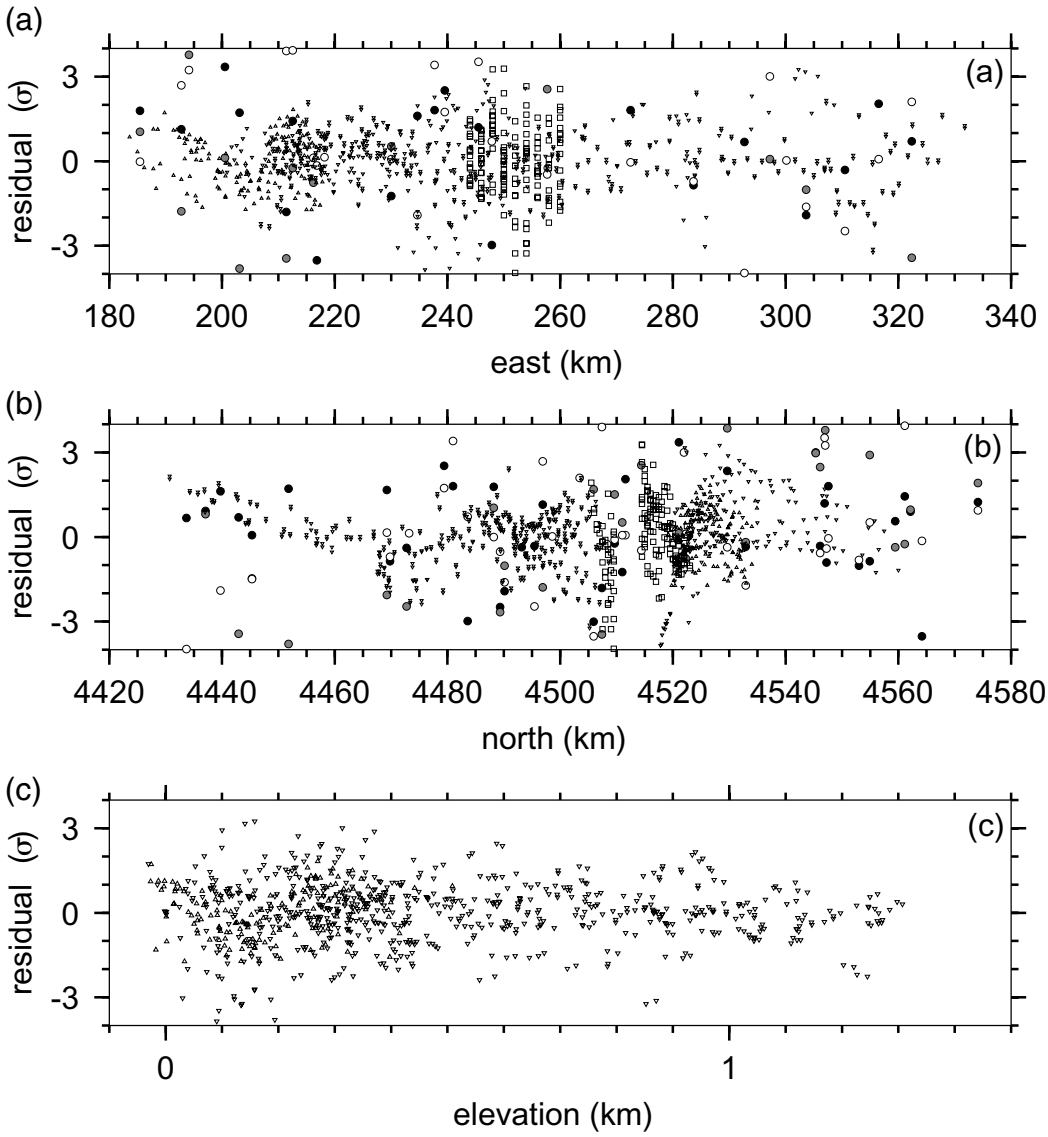

Figure 13. Profiles along (a) east, (b) north, and (c) vertical axes of normalized residuals for the EGS inversion, showing ERS-1 range changes (downward-pointing triangles), showing RADARSAT range changes (upward-pointing triangles), GPS displacements (white, gray, and black circles for east, north, and up components, respectively), and SPOT offsets (squares).

displacement field, which are in turn sensitive to errors in range along the steep line-of-sight used by the ERS radar. In the far field, at 50 km from the fault, an error of one 28-mm fringe in range can alter the estimate of slip on the fault by several meters.

In our *ERGS* inversion, the correlation of E range change with topography is strong, yielding a vertical gradient of $\partial(\Delta\rho)/\partial z = 25 \pm 3$ mm in range per kilometer of elevation. This produces more than a fringe in the valley around İzmit, just as in the aseismic one-day interferogram (Fig. 3). Estimating this nuisance parameter yields a moment only 1% different than the moment estimated in a solution where we neglect the tropospheric gradient. On the other hand, one parameter may not suffice to describe the troposphere over the entire 100- by 150-km interferogram. For example, the steep slope in the eastern half of the GPS–ERS range differences (Fig. 2) suggests an eastward gradient of 50 mm in range over 10 km or $\partial(\Delta\rho)/\partial x \sim 5 \times 10^{-6}$ that may be related to localized heterogeneities in the troposphere. Similarly, at least one of the fringes remaining in the residual interferogram (Fig. 14) may be a tropospheric perturbation over a length scale shorter than the entire 100-km-wide image. We conclude that short-scale tropospheric variations appear to be the dominant source of error contributing to the ~2 cm uncertainty we find for the E measurements.

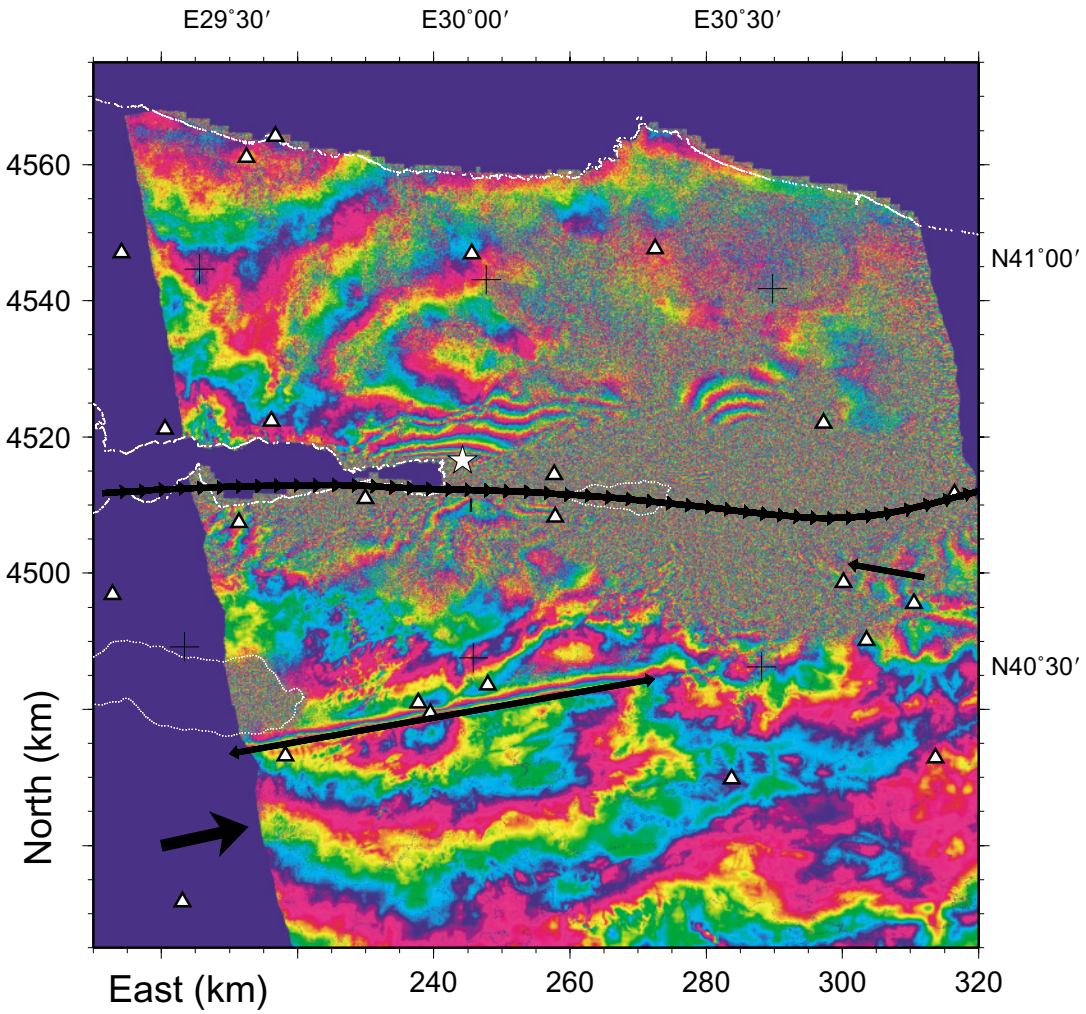

Figure 14. Residual (observed minus calculated) wrapped interferogram, shown as 28-mm fringes. The interferogram is calculated from ERS-1 SAR images taken before (12 August 1999) and after (16 September 1999) the Izmit earthquake. Each fringe denotes 28 mm of change in range. Here, the altitude of ambiguity h_a is 336 m. We cleaned the fringes with a power-spectrum filtering algorithm (Goldstein and Werner, 1998).

In contrast, the RADARSAT interferogram appears to have a negligible vertical gradient: $\partial(\Delta\rho)/\partial z = -2.1 \pm 0.2 \times 10^{-8}$, or less than 0.001 fringe per kilometer of topographic relief. Again, the limited spatial extent of the *R* data set is a caveat.

That the tropospheric noise in our RADARSAT interferogram is smaller than in the ERS-1 interferogram by at least a factor of 2 seems surprising in light of the similarity of the radar sensors. If anything, we would expect the opposite effect: the shallow incidence and daytime acquisition of the RADARSAT images should increase the tropospheric path delay and its variability with respect to ERS. Instead, we conclude that the tropospheric conditions vary greatly over short time scales (hours to days) and length scales (~10 km). In consequence, the uncertainties we derive from our *E* and *R* data sets may not apply to other INSAR measurements acquired under different atmospheric conditions.

Moment

Our estimate of the seismic moment from the *ERGS* inversion is only 8% larger than the estimate from strong-motion and teleseismic body-wave data (Yagi and Kikuchi, 2000). Yet our estimate is considerably smaller than others estimated from geodetic data sets, including some of the same ERS interferograms. For example, it is 22% to 25% smaller than that estimated by Wright *et al.* (2001), even after scaling to the same shear modulus. Similarly, our estimate of the moment is 16% smaller than that of Delouis *et al.* (2002), again after scaling to the same shear modulus.

Less than one-tenth of the discrepancy may be explained by the postseismic deformation, which amounts to 0.291×10^{20} N m in moment over the first 75 days following the mainshock, based on modeling of the GPS observations (Reilinger *et al.,* 2000). Although the ERS interfero-

grams record 30 days (0.1×10^{20} N m) of postseismic deformation, both Wright *et al.* (2001) and Delouis *et al.* (2002) neglect it.

The oversimplified assumption of uniform rheology implicit in our half-space model will tend to bias our moment estimate toward a low value. Using a realistic layered earth model, Hearn *et al.* (2002) find a moment of 2.6×10^{20} N m using the same GPS displacement vectors as we do. In other words, our moment estimate is 26% too low because we assume a uniform half-space.

Depth Estimates

Our geodetic estimates locate the centroid of the coseismic slip distribution at 11-km depth, shallower than seismological estimates of the mainshock centroid. This discrepancy has been observed before, for example, for the Northridge earthquake (Hudnut *et al.,* 1995). The explanation involves the differences in rheology assumed in the elastic modeling (Savage, 1987). For computational simplicity, our geodetic inversions assume an elastic half-space with constant properties throughout. Variations in crustal rheology clearly violate this assumption. For example, Hearn *et al.* (2002) found a centroid several kilometers deeper than ours by using a more realistic layered earth model.

Or, if the value of Poisson's ratio in the upper crust is lower than the $\nu = ¼$ value we assume, then the geodetic estimate will underestimate the depth, yielding a centroid location which is too shallow (Cattin *et al.,* 1999).

Oversimplifications in the Model

In comparing simple half-space models with more realistic layered rheologies, Hearn *et al.* (2002) found important differences in the ratio of vertical to horizontal components of displacement. Consequently, our elastic half-space model cannot adequately satisify both the GPS data, which are primarily horizontal, and the ERS and RADARSAT data, which are primarily vertical. This argument explains why the residual ERS interferogram calculated from the joint *ERGS* solution (Fig. 14) contains more fringes than that calculated from the *E* data set alone (not shown). The residual fringes in Figure 14 look as if they were made by an earthquake. Fitting them, without trading slip for nuisance parameters, would tend to increase the moment estimate. This argument explains why Wright *et al.* (2002) estimate a 50% larger value for moment than we do when fitting the same ERS-1 interferogram alone.

Secondary Rupture off the Main Trace

Using the fault geometry chosen to fit the ERS interferograms (Wright *et al.,* 2001), we find 116 ± 12 mm of right-lateral strike slip and 35 ± 12 mm of thrusting up-dip slip between 0.3 and 14.7 km depth on a 10-km-long fault that dips 50° N and strikes N80°W in the Mudurnu Valley. Near Lake Iznik, we find 227 ± 20 mm of left-lateral strike slip and 170 ± 23 mm of dip slip between 2.5- and 3.5-km depth on a 60-km-long vertical fault that strikes S80°W. These modeled fault values fit the ERS data poorly, as apparent in the residual interferogram (Fig. 14). Obtaining a better fit would require adjusting the modeled fault geometry in a nonlinear inversion, a task beyond the scope of this article.

How Far Does the Rupture Continue beyond the Hersek Delta?

At the western termination of the fault, near the Hersek delta, the location of the 1-m slip contour depends on the relative geometry of the data sampling and the fault parameterization. In our *G* solution, the GPS data alone place this contour some 9 km west of the delta tip, while the ERS and RADARSAT data sets place it 13 to 15 km west of the delta in the *E* and *R* solutions. Further west, the slip tapers off gradually from 2 m to 1 m in the 10 km past the delta. Our joint *EGS* inversion, dominated by the GPS data, places the 1-m slip contour 9 km west of the tip of the Hersek delta. At the end of our model fault, 20 km west of the Hersek delta, the slip diminishes to zero. Such a shallow gradient of slip reduces the stress accumulating at the tip of the fault.

Further west, between 20 and 35 km beyond the delta, where Karabulut *et al.* (2001) found aftershock activity including two events with $M_w > 4$, our solutions do not resolve any significant coseismic slip at the meter level. This suggests that the observed aftershocks represent minor ($\sim$1 cm) adjustments induced at the fault tip by the mainshock rather than throughgoing coseismic slip. Still, even $\sim$10 cm of slip in this area would not appear in our solutions because of the lack of geodetic data offshore and the no-slip boundary condition we impose at the end of the modeled fault.

At this western termination of the fault, our slip distribution appears to be roughly consistent with those of other studies to within the real 1-m errors of the inversions. For example, the 2-m slip contour in our *ERGS* solution at 10-km depth falls 40 km west of the hypocenter. It resembles the results of an inversion of strong-motion data alone (Bouchon *et al.,* 2001). Below this depth, this contour curves eastward, back toward the hypocenter, in our geodetic solution, whereas it dips westward in the strong-motion solution, presumably because of our bottom boundary condition and smoothing constraint.

Differences in geometric parameterization of the fault model can also effect the slip distribution, especially at the western offshore termination where no surface rupture mapping is available. Finally, the nuisance parameters required for modeling the ERS data trade off with the fault slip parameters, whether the former are explicitly estimated (as in this study), modeled physically using precise orbits (Wright *et al.,* 2001), or absorbed into baseline estimation (Delouis *et al.,* 2002).

Given the differences between the various models, we conclude that the slip distributions include errors at the level of at least 1 m, considerably larger than the 0.2-m standard deviations we determine formally by linear propagation of the measurement uncertainties. Accordingly, the prudent geophysical conclusion is that coseismic slip during the İz-

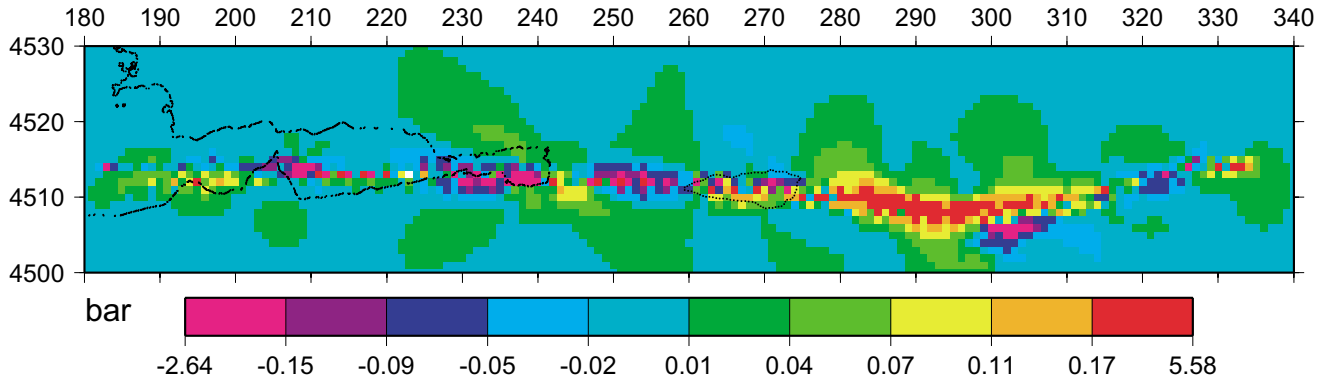

Figure 15. Map of difference in Coulomb failure stress increase between two assumptions for the slip distribution: that estimated from GPS alone (Reilinger *et al.,* 2000) minus that estimated in our ERGS joint inversion.

mit earthquake tapers gradually from 2 m under the Hersek delta to 1 m at a point 10 km west of it.

Sensitivity of Stress Transfer Calculations to Slip Distribution

At Landers, we learned a lesson about how the change in Coulomb failure stress depends on the slip distribution assumed in the calculation. By using a fine estimate of slip distribution estimated from several data sources (Wald and Heaton, 1994), Stein *et al.* (1994) predict aftershock locations better than with their original calculation (Stein *et al.,* 1992) that used only a coarse estimate of slip distribution based on GPS measurements alone (Murray *et al.,* 1993). Yet even the most recent Coulomb calculations do not predict exactly where the triggered slip begins and ends (Massonnet *et al.,* 1994; Price and Sandwell, 1998).

For İzmit, the first two triggering studies (Hubert-Ferrari *et al.,* 2000; Parsons *et al.,* 2000) relied on unpublished, preliminary estimates of the slip distribution. To illustrate the sensitivity, we calculated the Coulomb failure stress perturbation twice: first using the slip distribution estimated from the GPS data alone by Reilinger *et al.* (2000) on the six-segment geometry and then using our *ERGS* estimate on the smooth geometry (Fig. 15). Near the fault, where a future earthquake is likely to nucleate, the differences exceed 0.5 bar, the conventional threshold for triggering an earthquake.

Conclusions

We have combined three distinct types of geodetic data that measure six different components of the coseismic displacement field. For the ERS-1 range changes, a standard deviation of 22 mm in range is appropriate, provided that we admit the possibility of gradients in the eastward, northward, and upward directions. Our estimates for all these gradients are significant, of the order of approximately 1 mm/km horizontally and approximately 25 mm/km vertically. These represent residual orbital and tropospheric effects, respectively. For the small subset of the RADARSAT interferogram we use, the standard deviation is smaller, about 12 mm. Although the horizontal gradients in the RADARSAT data are of the same order of magnitude as those in the ERS data, the vertical gradients appear to be negligible. For the offsets estimated by correlating SPOT images, 63 cm is appropriate for the standard deviation of a 2- by 2-km sample.

After accounting for a month's postseismic deformation, we have used these data to estimate the distribution of slip at the instant of the İzmit mainshock. The moment M_0 is 1.84×10^{20} N m, and the moment magnitude M_w is 7.50. Although this value is within 10% of an estimate from seismometer data alone (Yagi and Kikuchi, 2000), it is over 25% smaller than the values estimated from other inversions. The primary cause for this discrepancy is the rheological oversimplification implicit in our half-space model. Other possible explanations for the discrepancy involve neglecting postseismic deformation, tropospheric artifacts, or orbital gradients. Although our joint inversion of the different geodetic data sets accounts for all these effects, they do not seem to modify the moment by more than about 5%.

We find that a smooth fault geometry fits the geodetic data better than a stepping arrangement of linear segments. We hypothesize that the fault is a single, well-connected surface at depth.

The joint inversion of four different geodetic data sets resolves features of the slip distribution the level of 1 m. At the western end of the rupture, where the risk to Istanbul depends on the stress accumulation, the prudent geophysical conclusion is that coseismic slip during the İzmit earthquake tapers gradually from 2 m under the Hersek delta to 1 m at a point 10 km west of it. Our solution cannot resolve any significant slip beyond 10 km west of the Hersek delta. Accordingly, we infer that the Yalova segment to the west of the Hersek delta may remain capable of significant slip in a future earthquake.

A reliable estimate of the slip distribution is important for stress transfer calculations. Subtle differences between two acceptable, and apparently similar, slip distributions can perturb the Coulomb failure stress increment by more than

the threshold value usually considered sufficient to trigger an earthquake.

Acknowledgments

We thank Ziyadin Çakir and Aykut Barka of ITU for precious assistance in the field. We also appreciated the guidance kindly offered by Bob King and Tom Herring of MIT. Eric Fielding selflessly released his DEM early. Tim Wright and Barry Parsons generously provided results in advance of publication. A thorough review by Eric Fielding and Tim Wright improved the manuscript considerably. Geoff King offered helpful guidance as well as his Almond source code. Zhong Lu generously adapted his ps_filt2 program to clean our fringes. Edmond Nezry of Privateers helped with the ERS correlation. John Dow and Matt Rosengren responded quickly to control and determine the ERS orbits from ESA/ESOC. Betlem Rosich-Tell and Alain Arnaud of ESA/ESRIN accelerated the data distribution. Alain Podaire of CNES astutely recognized the importance of this event. Paul Wessel and Walter Smith's terrific GMT software (Wessel and Smith, 1998) illustrated the article with the exception of Figure 2. We acknowledge the European Space Agency for providing the ERS data free of cost and the Canadian Space Agency for providing the RADARSAT data free of charge under ADRO2 and the background mission. Financed by *l'Institut National des Sciences de l'Univers,* GDR INSAR, and CNES/QTIS in France, and NSF grant EAR 9909730 to M.I.T.

References

Anderson, E., Z. Bai, C. Bischof, J. Demmel, J. Dongarra, J. Du Croz, A. Greenbaum, S. Hammarling, A. McKenney, S. Ostrouchov, and D. Sorenson (1992). *LAPACK Users' Guide*, Society for Industrial and Applied Mathematics, Philadelphia.

Armijo, R., B. Meyer, A. Barka, J. B. de Chabalier, and A. Hubert-Ferrari (1999). The 1999 İzmit earthquake rupture and the tectonic evolution of the Sea of Marmara, *EOS* **80,** F664.

Ayhan, M. E., R. Bürgmann, S. McClusky, O. Lenk, B. Aktug, E. Herece, and R. E. Reilinger (2001). Kinematics of the M_w = 7.2, 12 November 1999, Düzce, Turkey earthquake, *Geophys. Res. Lett.* **28,** 367–370.

Ayhan, M. A., C. Demir, A. Kiliçoglu, I. Sanli, and S. M. Nakiboglu (1999). Crustal motion around the western segment of the north Anatolian fault zone: geodetic measurements and geophysical interpretation, *in International Union of Geodesy and Geophysics,* Birmingham, U.K.

Bamler, R., and P. Hartl (1998). Synthetic aperture radar interferometry, *Inverse Problems* **14,** R1–R54.

Barka, A. (1999). The 17 August 1999 İzmit earthquake, *Science* **285,** 1858–1859.

Barka, A., S. Akyuz, E. Altunel, G. Sunal, Z. Cakir, A. Dikbas, B. Yerli, T. Rockwell, J. Dolan, T. Dawson, R. Hartleb, A. Tucker, T. Fumal, R. Langridge, H. Stenner, S. Christofferson, R. Armijo, B. Meyer, and J. B. Chabalier (1999). 17 August 1999 İzmit earthquake, northwestern Turkey, *EOS* **80,** F647.

Barrientos, S. E., and S. N. Ward (1990). The 1960 Chile earthquake: inversion for slip distribution from surface deformation, *Geophys. J. Int.* **103,** 589–598.

Beauducel, F., P. Briole, and J. L. Froger (2000). Volcano wide fringes in ERS synthetic aperture radar interferograms of Etna: deformation or tropospheric effect? *J. Geophys. Res.* **105,** 16,391–16,402.

Bouchon, M., M. N. Toksöz, H. Karabalut, M. P. Bouin, M. Dietrich, M. Aktar, and M. Edie (2002). Space and time evolution of rupture and faulting during the 1999 İzmit (Turkey) earthquake, *Bull. Seism. Soc. Am.* **92,** no. 1, 256–266.

Bürgmann, R., M. E. Ayhan, E. Fielding, T. Wright, S. McClusky, B. Aktug, C. Demir, O. Lenk, and A. Türkezer (2002). Deformation during the 12 November 1999, Düzce, Turkey, Earthquake, from GPS and InSAR Data, *Bull. Seism. Soc. Am.* **92,** no. 1, 161–171.

Bürgmann, R., P. A. Rosen, and E. J. Fielding (2000). Synthetic aperture radar interferometry to measure Earth's surface topography and its deformation, *Annu. Rev. Earth Planet. Sci.* **28,** 169–209.

Çakır, Z., J. B. d. Chabalier, R. Armijo, B. Meyer, A. Barka, and G. Peltzer (2001). The August 17, 1999 Turkey earthquake seen with InSAR imagery and tectonic field observations, presented at the European Union of Geosciences XI Meeting, Strasbourg, France.

Cattin, R., P. Briole, H. Lyon-Caen, P. Bernard, and P. Pinettes (1999). Effects of superficial layers on coseismic displacements for a dip-slip fault and geophysical implications, *Geophys. J. Int.* **137,** 149–158.

Çemen, I., E. Gökten, B. Varol, R. Kiliç, V. Özaksoy, and C. Erkmen (2000). Turkish earthquakes reveal dynamics of fracturing along a major strike-slip fault zone, *EOS* **81,** no. 11, 309–313.

Centre National d'Etudes Spatiales (CNES) (1997). DIAPASON software package, CNES, Toulouse, France.

Crippen, R. E. (1992). Measurement of subresolution terrain displacements using SPOT panchromatic imagery, *Episodes* **15,** 56–61.

Crippen, R. E., and R. G. Blom (1992). The first visual observation of fault movements from space, the 1992 Landers Earthquake, *EOS* **73,** 364.

Delacourt, C., P. Briole, and J. Achache (1998). Tropospheric corrections of SAR interferograms with strong topography: application to Etna, *Geophys. Res. Lett.* **25,** 2849–2852.

Delouis, B., D. Giardini, P. Lundgren, and J. Salichon (2002). Joint inversion of INSAR, GPS, teleseismic, and strong-motion data for the spatial and temporal distribution of earthquake slip: application to the 1999 İzmit mainshock, *Bull. Seism. Soc. Am.* **92,** no. 1, 278–299.

Ergintav, S., R. Bürgmann, S. McClusky, R. Çakmak, R. E. Reilinger, O. Lenk, A. Barka, and H. Özener (2002). Postseismic deformation near the İzmit earthquake (17 August 1999, *M* 7.5) rupture zone, *Bull. Seism. Soc. Am.* **92,** no. 1, 194–207.

Feigl, K. L. (2002). Measurement of coseismic deformation by satellite geodesy, in *International Handbook of Earthquake and Engineering Seismology,* W. H. K. Lee, H. Kanamoori, and P. C. Jennings, (Editors), Academic Press, San Diego (in press).

Feigl, K. L., and E. Dupré (1999). RNGCHN: a program to calculate displacement components from dislocations in an elastic half-space with applications for modeling geodetic measurements of crustal deformation, *Computers and Geosciences* **25,** 695–704.

Fielding, E., T. Wright, B. Parsons, P. England, P. Rosen, S. Hensley, and R. Bilham (1999). Topography of northwest Turkey from SAR interferometry. Application to the 1999 İzmit earthquake: geomorphology and coseismic strain, *EOS* **80,** F663.

Goldstein, R. (1995). Atmospheric limitations to repeat-track radar interferometry, *Geophys. Res. Lett.* **22,** 2517–2520.

Goldstein, R. M., and C. L. Werner (1998). Radar interferogram filtering for geophysical applications, *Geophys. Res. Lett.* **25,** no. 21, 4035–4038.

Hanssen, R. (1998). Atmospheric heterogeneities in ERS tandem SAR interferometry, Delft University Press, Delft, The Netherlands, 136.

Hanssen, R. F. (2001). *Radar Interferometry: Data Interpretation and Analysis, Remote Sensing and Digital Image Processing,* Kluwer Academic Publishers, Dordrecht.

Hearn, E. H., R. Burgmann, and R. E. Reilinger (2002). Dynamics of İzmit earthquake postseismic deformation and loading of the Düzce earthquake hypocenter, *Bull. Seism. Soc. Am.* **92,** no. 1, 172–193.

Herring, T. A. (1991). GLOBK: Global Kalman filter VLBI and GPS analysis program, Massachusetts Institute of Technology, Cambridge.

Holdahl, S. R., and J. Sauber (1994). Coseismic slip in the 1964 Prince William Sound earthquake: a new geodetic inversion, *Pageoph* **142,** 55–82.

Hubert-Ferrari, A., A. Barka, E. Jacques, S. S. Nalbant, B. Meyer, R. Armijo, P. Tapponnier, and G. C. P. King (2000). Seismic hazard in the

Marmara Sea region following the 17 August 1999 İzmit earthquake, *Nature* **404,** 269–273.

Hudnut, K. W., Z. Shen, M. Murray, S. McClusky, R. King, T. Herring, B. Hager, Y. Feng, P. Fang, A. Donnellan, and Y. Bock (1995). Coseismic displacements of the 1994 Northidge, California earthquake, *Bull. Seism. Soc. Am.* **86,** no. 1B, S49–S70.

Karabulut, H., M. P. Bouin, M. Bouchon, M. Dietrich, C. Cornu, and M. Aktar (2002). The seismicity in the Eastern Marmara Sea after the 17 August 1999 İzmit earthquake, *Bull. Seism. Soc. Am.* **92,** no. 1, 387–393.

King, R. W., and Y. Bock (1997). Documentation for the MIT GPS Analysis Software: GAMIT, Massachusetts Institute of Technology, Cambridge.

Madsen, S. N., and H. A. Zebker (1998). Imaging radar interferometry, in *Principles and Applications of Imaging Radar: Manual of Remote Sensing,* F. M. Henderson and A. J. Lewis (Editors), Wiley, New York, 359–380.

Massonnet, D., and K. L. Feigl (1995). Discriminating geophysical phenomena in satellite radar interferograms, *Geophys. Res. Lett.* **22,** 1537–1540.

Massonnet, D., and K. L. Feigl (1998). Radar interferometry and its application to changes in the Earth's surface, *Rev. Geophys.* **36,** no. 4, 441–500.

Massonnet, D., and T. Rabaute (1993). Radar interferometry: limits and potential, *IEEE Trans. Geosci. Rem. Sensing* **31,** 455–464.

Massonnet, D., P. Briole, and A. Arnaud (1995). Deflation of Mount Etna monitored by spaceborne radar interferometry, *Nature* **375,** 567–570.

Massonnet, D., K. L. Feigl, M. Rossi, and F. Adragna (1994). Radar interferometric mapping of deformation in the year after the Landers earthquake, *Nature* **369,** 227–230.

Massonnet, D., M. Rossi, C. Carmona, F. Adragna, G. Peltzer, K. Feigl, and T. Rabaute (1993). The displacement field of the Landers earthquake mapped by radar interferometry, *Nature* **364,** 138–142.

McClusky, S., S. Balassanian, A. Barka, C. Demir, S. Ergintav, I. Georgiev, O. Gurkan, M. Hamburger, K. Hurst, H. Kahle, K. Kastens, G. Kekelidze, R. King, V. Kotzev, O. Lenk, S. Mahmoud, A. Mishin, M. Nadariya, A. Ouzounis, D. Paradissis, Y. Peter, M. Prilepin, R. Reilinger, I. Sanli, H. Seeger, A. Tealeb, M. N. Toksöz, and G. Veis (2000). Global Positioning System constraints on plate kinematics and dynamics in the eastern Mediterranean and Caucasus, *J. Geophys. Res.* **105,** no. B3, 5695–5720.

Menke, W. (1989). *Geophysical Data Analysis: Discrete Inverse Theory,* International Geophysics Series, Academic Press, San Diego, 289.

Michel, R., J. P. Avouac, and J. Taboury (1999). Measuring ground displacements from SAR amplitude images: application to the Landers earthquake, *Geophys. Res. Lett.* **26,** 875–878.

Murray, M. H., J. C. Savage, M. Lisowski, and W. K. Gross (1993). Coseismic displacements: 1992 Landers, California earthquake, *Geophys. Res. Lett.* **20,** 623–626.

Okada, Y. (1985). Surface deformation to shear and tensile faults in a half-space, *Bull. Seism. Soc. Am.* **75,** no. 4, 1135–1154.

Parsons, T., S. Toda, R. S. Stein, A. Barka, and J. H. Dieterich (2000). Heightened odds of large earthquakes near Istanbul: an interaction-based probability calculation, *Science* **288,** no. 5466, 661–665.

Price, E. J., and D. T. Sandwell (1998). Small-scale deformations associated with the 1992 Landers, California, earthquake mapped by synthetic aperture radar interferometry phase gradients, *J. Geophys. Res.* **103,** no. B11, 27,001–27,016.

Reilinger, R. E., S. Ergintav, R. Bürgmann, S. McClusky, O. Lenk, A. Barka, O. Gurkan, L. Hearn, K. L. Feigl, R. Cakmak, B. Aktug, H. Ozener, and M. N. Toksöz (2000). Coseismic and postseismic fault slip for the 17 August 1999, M = 7.4, İzmit, Turkey earthquake, *Science* **289,** 1519–1524.

Rigo, A., and D. Massonnet (1999). Investigating the 1996 Pyrenean earthquake (France) with SAR Interferograms heavily distorted by atmosphere, *Geophys. Res. Lett.* **26,** 3217–3220.

Rosen, P. A., S. Hensley, H. A. Zebker, F. H. Webb, and E. J. Fielding (1996). Surface deformation and coherence measurements of Kilauea volcano, Hawaii from SIR-C radar interferometry, *J. Geophys. Res.* **101,** 23,109–23,125.

Sarti, F., E. Nezry, and F. Adragna (2000). Complentarity of correlation and interferometry for the analysis of the effects of the İzmit earthquake with radar data, in *Proc. 6th International Conference on Information Systems Analysis and Synthesis,* Orlando, Florida, 23–26 July 2000.

Savage, J. C. (1987). Effect of crustal layering upon dislocation modeling, *J. Geophys. Res.* **92,** 10595–10600.

Segall, P., and R. Harris (1987). Earthquake deformation cycle on the San Andreas fault near Parkfield, California, *J. Geophys. Res.* **92,** 10,511–10,525.

Snyder, J. P. (1982). Map projections used by the U.S. Geological Survey, *U.S. Geol. Surv. Bull. 313.*

Stein, R. S., G. C. P. King, and J. Lin (1992). Change in failure stress on the southern San Andreas fault system caused by the 1992 magnitude = 7.4 Landers earthquake, *Science* **258,** 1328–1332.

Stein, R. S., G. C. P. King, and J. Lin (1994). Stress triggering of the 1994 M = 6.7 Northridge, California earthquake by its predecessors, *Science* **265,** 1432–1435.

Straub, C., H.-G. Kahle, and C. Schindler (1997). GPS and geologic estimates of the tectonic activity in the Marmara Sea region, NW Anatolia, *J. Geophys. Res.* **102,** no. BB12, 27,587–27,602.

Tarayre, H., and D. Massonnet (1996). Atmospheric propagation heterogeneities revealed by ERS-1 interferometry, *Geophys. Res. Lett.* **23,** 989–992.

Vadon, H., and D. Massonnet (2000). Earthquake displacement fields mapped by very precise correlation: complementarity with radar interferometry, in *IEEE International Geoscience Remote Sensing Symposium,* Honolulu, Hawaii, 24–28 July 2000, IEEE Periodicals, Piscataway, New Jersey, 2700–2702.

Van Puymbroeck, N., R. Michel, R. Binet, J. P. Avouac, and J. Taboury (2000). Measuring earthquakes from optical satellite images, *Applied Optics* **39,** 3486–3494.

Wald, D. J., and T. H. Heaton (1994). Spatial and temporal distribution of slip for the 1992 Landers, California earthquake, *Bull. Seism. Soc. Am.* **84,** 668–691.

Wessel, P., and W. H. F. Smith (1998). New, improved version of generic mapping tools released, *EOS* **79,** no. 47, 579.

Williams, S., Y. Bock, and P. Fang (1998). Integrated satellite interferometry: tropospheric noise, GPS estimates, and implications for interferometric synthetic aperture radar products, *J. Geophys. Res.* **103,** no. B11, 27,051–27,068.

Wright, T. J., E. J. Fielding, B. E. Parsons, and P. C. England (2001). Triggered slip: observations of the 17 August 1999 İzmit (Turkey) earthquake using radar interferometry, *Geophys. Res. Lett.* **28,** 1079–1082.

Yagi, Y., and M. Kikuchi (2000). Source rupture process of the Kocaeli, Turkey earthquake of August 17, 1999 obtained by joint inversion of near-field data and teleseismic data, *Geophys. Res. Lett.* **27,** 1969–1972.

Yalcin, N., S. Ergintav, M. Aktar, C. Gurbuz, O. Gurkan, H. Eyidogan, A. E. A. Barka, O. Lenk, R. Reilinger, and M. N. Toksöz (1999). Seismic hazard assessment in the Marmara Sea region, in *International Union of Geodesy and Geophysics,* Birmingham, U.K.

Zebker, H. A., P. A. Rosen, and S. Hensley (1997). Atmospheric effects in interferometric synthetic aperture radar surface deformation and topographic maps, *J. Geophys. Res.* **102,** 7547–7563.

Department of Terrestrial and Planetary Dynamics (UMR 5562)
Centre National de la Recherche Scientifique
14 ave. E. Belin, 31400 Toulouse, France
Kurt.Feigl@cnes.fr
(K.L.F., A.R.)

Centre National d'Etudes Spatiales (CNES)
18 ave. E. Belin, 31401 Toulouse, France
Francesco, Sarti@cnes.fr, Helene.Vadon@cnes.fr, Philippe.Durand@cnes.fr, Didier Massonet@cnes.fr
(F.S., H.V., P.D., D.M.)

Department of Earth, Atmospheric, and Planetary Sciences
Massachusetts Institute of Technology
E34, 42 Carleton Street
Cambridge, Massachusetts, 02142
simon@wegener.mit.edu, reilinge@erl.mit.edu
(S.M., R.R.)

TUBITAK, Marmara Research Center, ESRI,
Gebze 41470, Turkey
semih@yunus.mam.gov.tr
(S.E.)

Department of Earth and Planetary Science
307 McCone Hall, University of California, Berkeley
Berkeley, California, 94720
burgmann@seismo.berkeley.edu
(R.B.)

Manuscript received 15 September 2000.